TAMPEREEN TEKNILLINEN YLIOPISTO
TAMPERE UNIVERSITY OF TECHNOLOGY

LIONEL HULTTINEN

POSITION-BASED IMPEDANCE CONTROL OF A HYDRAULIC ROCK BREAKER BOOM

Master of Science thesis

Examiners: Prof. Jouni Mattila,
D. Sc. Janne Koivumäki
Examiners and topic approved by the
Faculty Council of the Faculty of
Engineering Sciences
on 9th August 2017

ABSTRACT

LIONEL HULTTINEN: Position-based impedance control of a hydraulic rock breaker boom
Tampere University of Technology
Master of Science thesis, 50 pages, 9 Appendix pages
November 2017
Master's Degree Programme in Automation Technology
Major: Fluid Power Automation
Examiners: Professor Jouni Mattila, Doctor of Science Janne Koivumäki
Keywords: rock breaker boom, hydraulic manipulator, impedance control

This thesis considers the automatization of a rock breaker boom equipped with a hydraulic hammer. The studied use case of an automatized breaker boom consists of trajectory generation from a standby position to preprogrammed locations on a steel grid. The operator shall be able to choose a specific location of the grid from a user interface and the boom shall automatically move above the chosen location, do an approach movement towards the grid and switch the hydraulic hammer on when contact with an external object is detected. During this sequence the angle of the rock hammer should be constantly maintained at vertical orientation relative to the grid.

The developed solution for contact detection is based on impedance control, which is a form of indirect force control built on top of an underlying operational-space tool centre control scheme. To implement impedance control for hydraulic manipulators, pressure sensors and knowledge of boom kinematics and dynamics are necessary. In its simplest form, modeled configuration-dependent gravitational forces affecting the hydraulic cylinders are subtracted from pressure readings and mapped into forces affecting in Cartesian space to yield a rough estimate of contact forces affecting on the manipulator. The estimated contact forces are then filtered into a position modification that indirectly regulates the force affecting on the tool tip of the manipulator. The force tracking performance is dependent on the underlying position controller, which is why the control scheme is referred to as position-based impedance control.

In this thesis, an impedance controller was developed for a four degrees-of-freedom hydraulic manipulator and it was verified using a simulation model of the manipulator. The sequence was implemented on the actual breaker plant and a simple position controller was tuned, but the original objective of identifying dynamic parameters and testing of the impedance controller for contact detection as a part of the automatic sequence was not met.

TIIVISTELMÄ

LIONEL HULTTINEN: Hydraulisen kivenrikotuspuomin asemapohjainen impedanssisäätö
Tampereen teknillinen yliopisto
Diplomityö, 50 sivua, 9 liitesivua
Marraskuu 2017
Automaatiotekniikan diplomi-insinöörin tutkinto-ohjelma
Pääaine: Fluid Power Automation
Työn ohjaajat: Professori Jouni Mattila, Tekniikan tohtori Janne Koivumäki
Avainsanat: kivenrikotuspuomi, hydraulinen manipulaattori, impedanssisäätö

Tämä diplomityö käsittelee hydraulivasaralla varustetun kivenrikotuspuomin automatisointia. Tutkittu käyttötapaus koostuu liikeratojen muodostamisesta alkuasennosta ennaltamääriteltyihin pisteisiin metalliristikolla. Koneenkäyttäjän tulee kyetä valitsemaan käyttöliittymästä haluttu sijainti ristikolla, jolloin puomi paikottaa itsensä kyseisen aseman yläpuolelle, tekee lähestymisliikkeen kohti ristikkoa ja kytkee hydraulivasaran päälle havaitessaan kontaktin ulkoisen esteen kanssa. Koko sekvenssin aikana kivivasaran orientaatio tulee pitää kohtisuorana ristikkoon nähden.

Kontaktin havaitsemiseen kehitetty ratkaisu perustuu impedanssisäätöön, joka on asemasäätimen pohjalle rakennettu epäsuora voimasäädin. Impedanssisäädön toteuttaminen hydraulisille puomeille vaatii tyypillisesti paineanturointia sekä puomin kinematiikan ja dynamiikan tuntemusta. Yksinkertaisimmillaan tunnetut hydraulisylintereihin vaikuttavat asemariippuvaiset gravitaatiovoimat vähennetään painemittauksista ja muunnetaan karteesisessa avaruudessa vaikuttaviksi voimakomponenteiksi, jolloin saadaan karkea arvio puomiin vaikuttavista ulkoisista voimista. Voimaestimaatti suodatetaan tämän jälkeen asemareferenssiä poikkeuttavaksi asemamyödöksi, mikä epäsuorasti säätelee puomin kärkeen kohdistuvia voimia. Voiman regulointitarkkuus riippuu puomin asemasäätimen suorituskyvystä, minkä johdosta säätörakennetta kutsutaan asemapohjaiseksi impedanssisäädöksi.

Työssä kehitettiin impedanssisäädin neljän vapausasteen hydrauliselle puomille ja sen toiminta verifioitiin puomin simulointimallia käyttäen. Sekvenssi toteutettiin todelliselle puomille ja puomille viritettiin yksinkertainen asemasäädin, mutta työn alkuperäisestä tavoitteesta poiketen puomin dynaamisten parametrien identifiointi sekä impedanssisäätimen testaaminen kontaktin havaitsemiseen osana automaattista rikotussekvenssiä jäivät työn ulkopuolelle.

PREFACE

I would like to thank Prof. Mattila for the valuable experience and the persons stationed in room K2305 during these months for availability, help and guidance. In addition, I would like express my gratitude towards my parents for the care and support I've received before and during my studies.

Tampere, 22 November 2017

L. H.

CONTENTS

1. INTRODUCTION 1
1.1 Problem statement and use case description 2
1.2 Objective and structure of thesis 4
2. BOOM KINEMATICS AND DYNAMICS 5
2.1 Kinematic modeling of the manipulator 5
2.1.1 Inverse kinematics of X88-540R 7
2.1.2 Differential kinematics of X88-540R 8
2.2 Dynamic equation of the boom 10
3. IMPEDANCE SHAPING CONTROL 16
3.1 Cascaded compliance control 18
3.1.1 Position-based impedance control 20
3.1.2 Performance/robustness -tradeoff 21
3.1.3 Stability region of impedance parameters 23
3.2 Controller implementation 26
3.2.1 Pressure-based contact force estimation 28
3.2.2 Selection of impedance parameters 29
4. EXPERIMENTS AND RESULTS 32
4.1 Generation of the motion sequence 33
4.2 Tuning of the position controller 35
5. SUMMARY AND CONCLUSIONS 46
REFERENCES 50
APPENDIX A: Matlab-code for inverse arm dynamics 51
APPENDIX B: Tracking performance for target points 53

LIST OF ABBREVIATIONS AND SYMBOLS

COM	centre of mass
DOF	degree of freedom
DH	Denavit-Hartenberg
FBIC	force-based impedance control
IIR	infinite impulse response
PBIC	position-based impedance control
TOF	time of fligth

A_1, A_2	effective pressure areas of cylinder piston and rod
b_d	value of desired damping
$\mathbf{J}$	Jacobian matrix from cylinder extension to end-effector location
$\mathbf{J}_c$	Jacobian matrix from joint angle to cylinder extension
$\mathbf{J}_x$	Jacobian matrix from joint angle to end-effector location
e_p	position control error
f_c	column vector of forces in actuator space
F_x	column vector of forces in operational space
F_0	nominal force reference in operational space
$\widehat{F}_{ext}$	estimated contact forces in operational space
$\mathbf{G}$	gravity vector of the manipulator
$\mathbf{I}$	inertia matrix of the manipulator
k_d	value of desired stiffness
m	link mass
m_d	value of desired inertia
p_1, p_2	pressures affecting cylinder piston and rod areas
s	Laplace variable
$\mathbf{T}$	transformation matrix
u	valve control input
x_0	nominal position reference in operational space
x_{ref}	actual position reference in operational space
x_{mod}	position modification in operational space
$\mathbf{Y}$	regressor matrix
Z_E	environment impedance
Z_T	target impedance
θ	column vector of joint angles
$\dot{\theta}$	column vector of joint velocities
$\ddot{\theta}$	column vector of joint accelerations

τ	time constant of low-pass filter
$\boldsymbol{\tau}$	column vector of joint torques
ϕ	orientation angle of the tool relative to ground
φ	parameter vector
$\mathcal{L}$	Lagrangian
$\mathcal{K}$	kinetic energy
$\mathcal{P}$	potential energy
ω	natural frequency
ζ	damping ratio

1. INTRODUCTION

Booms equipped with hydraulic impact hammers are extensively used in the mining industry for controlled size reduction of mineral ore, most notably in close proximity of mobile jaw crushers and mining ore silos. These so called breaker booms (see Fig. 1.1) are essential to handle inevitably occuring material buildups and blockages caused by too coarse material that gets stuck on a screening media (i.e. a steel grate, also called a grizzly) while being fed to crushers or ore passes. The material that cannot pass through the openings of the screening media should be broken with the hydraulic hammer. This process is referred to as screening and is an essential step in crushing, turning unprocessed run-of-mine ore into a finer substance suitable for further treatment. [Metso Mining and Construction, 2015]

Figure 1.1 *A pedestal hydraulic rock breaker boom.* [`http://mrbbooms.com/`]

The economical justification for such booms is to reduce delays and ensure a steady material flow, leading to minimal process downtime and thereby having a positive impact on productivity. Whenever oversized rocks are caught on the grizzly structure, the rock hammer is used to reduce their size. This temporarily halts the material flow, for example when an ore truck has to stop feeding material to the silo

until the operator of the breaker boom has broken the oversized rocks into smaller particles that can pass trough the grizzly. If the boom cannot execute its task during a limited time window, the rock has to be temporarily pushed aside from the grid for later processing and the arm should return to rest position. Rock breaker booms are currently mostly operated by manual open-loop control each joint separately, making them inergonomic and non-intuitive to use from the point of view of the operator, which increases accident-proneness. Operator-induced accidents account for almost three out of four out of all crane accidents [Lovgren, 2004].

As for other applications, heavy-duty hydraulic manipulators on non-road mobile machinery (e.g. agriculture, construction and forestry) have seen developments of robotization in an increasing degree during the last years. Examples include John Deere *Intelligent Boom Control*[1] in forestry cranes and HIAB *Crane Tip Control*[2] in loader cranes, which both provide the operator with the opportunity to control the tool tip of the boom instead of separate joint control. Such coordinated operational-space control schemes are expected to decrease the cognitive burden of the operator, providing comfort and ease of operation. These recent developments indicate that there is room for improvement and open possibilities to apply robotic control in order to automatize rock breaking tasks, with the aim of making breaker booms safer, faster and more efficient.

1.1 Problem statement and use case description

A critical issue in rock breaking is to make contact with the rock in a controlled manner and applying a correct force, which requires a skilled operator. The hammer tip should be held in a 90 degree angle relative to the object (see Fig. 1.2) to avoid misalignment and nonideal distribution of impact forces. A lot of attention and effort goes into avoiding dangerous situations – for example, when the rock breaks, resulting idle strokes in air or collision with the ground can have a deteriorating effect on the hammer, shortening its lifespan. [Sandvik Mining and Construction, 2016]

Automatization of the breaker boom to solve the issues stated above requires the application of operational-space control and automatically generated motion trajectories. The studied use case for an automatized breaker boom is presented on the following page.

[1] See: `https://www.deere.com/en/forwarders/`

[2] See: `https://www.hiab.com/en/company/newsroom/news/hiab-crane-tip-control/` Accessed 10 November 2017

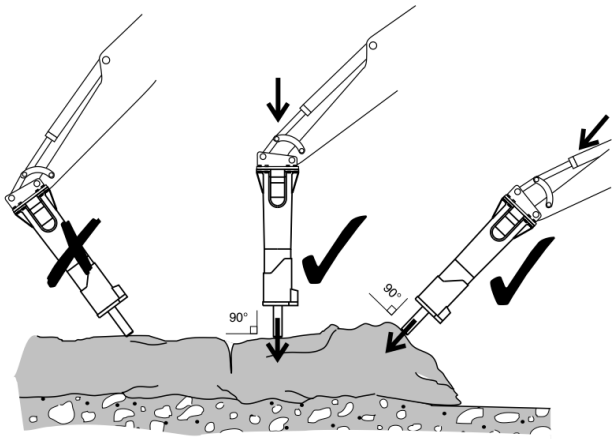

Figure 1.2 *Correct usage of the hammer. [Sandvik Mining and Construction, 2016]*

1. The boom has to automatically unfold itself from a rest position and move to a standby position beside the grid, the hammer being in a 90 degree orientation with respect to the grid.

2. In standby position, the operator should be able to choose a specific location of the grid from an intuitive graphical user interface, and the boom shall automatically move above that preprogrammed position with the angle of the rock hammer being constantly maintained at 90 degree vertical orientation relative to the grid.

3. The boom shall then do an approach move towards the grid maintaining the desired 90 degree tool orientation, and switch the rock hammer on when contact with an external object is detected. Special attention should be put into avoiding hitting the grid and not starting too far from the material's edge, which both could be equally detrimental for the equipment.

4. After having cleared the rock, the boom shall return to the rest position to wait for the next user commanded target.

The arising question in this use case is how to detect contact with a rock, since the hammer should automatically start its operation before a certain force threshold is exceeded. In heavy-duty hydraulic booms, the usage of six degrees of freedom force and torque sensors is not feasible, since they are known to be sensitive to shocks and overloading [Koivumäki, 2016, p. 5]. Instead, either pressure sensors should be used for sensing external contact forces or inertial measurement units for detecting impacts. Another open question is whether it is necessary to provide some additional compliance by software for very fast movements of the boom, although the tip of the hydraulic hammer is equipped with a mechanical spring that complies in face of

obstacles. Fast movements of the boom could be an argument for using some form of contact control in addition to plain impact detection.

1.2 Objective and structure of thesis

The objective of this thesis is study the feasibility of impedance control in rock breaking applications. This thesis aims to develop an automatic rock breaking control scheme for a heavy-duty pedestal hydraulic rock breaker boom. The developed solutions should be based on either indirect force sensing by means of pressure transmitters or impact detection based on acceleration measurements from inertial measurement units attached to the links of the manipulator. The main question of research is whether active compliance would bring any added value to the rock breaking sequence.

This thesis consists of five chapters. In Chapter 2, kinematic and dynamic models of the boom are derived. Chapter 3 provides a general outlook on different approaches to impedance control, namely position-based impedance control and force-based impedance control, in the context of hydraulically actuated manipulators. It introduces the reader into the principles and concepts related to cascaded compliance control, including a comparison between the position-based and force-based approaches and their respective tradeoffs regarding stability and performance. A simplistic impedance control scheme for hydraulic manipulators is also presented. Chapter 4 presents measurements from experiments carried on the actual breaker boom plant. Finally, a summary of results together with conclusions is provided in Chapter 5.

2. BOOM KINEMATICS AND DYNAMICS

For the purpose of estimating contact forces from cylinder chamber pressures, an accurate model of the dynamic behaviour of the boom is needed. In this chapter the theoretical background will be provided for deriving forward kinematics following the Denavit-Hartenberg convention and manipulator dynamics following the Euler-Lagrange formulation, both standard practices in the field of robotics.

2.1 Kinematic modeling of the manipulator

Denavit-Hartenberg (DH) convention is followed to assign coordinate frames from the base to the tool center point, which allows expressing coordinate transforms by means of four parameters [Sciavicco et al., 2000, p. 42]. Frame assignment for the boom is illustrated in Figure 2.1.

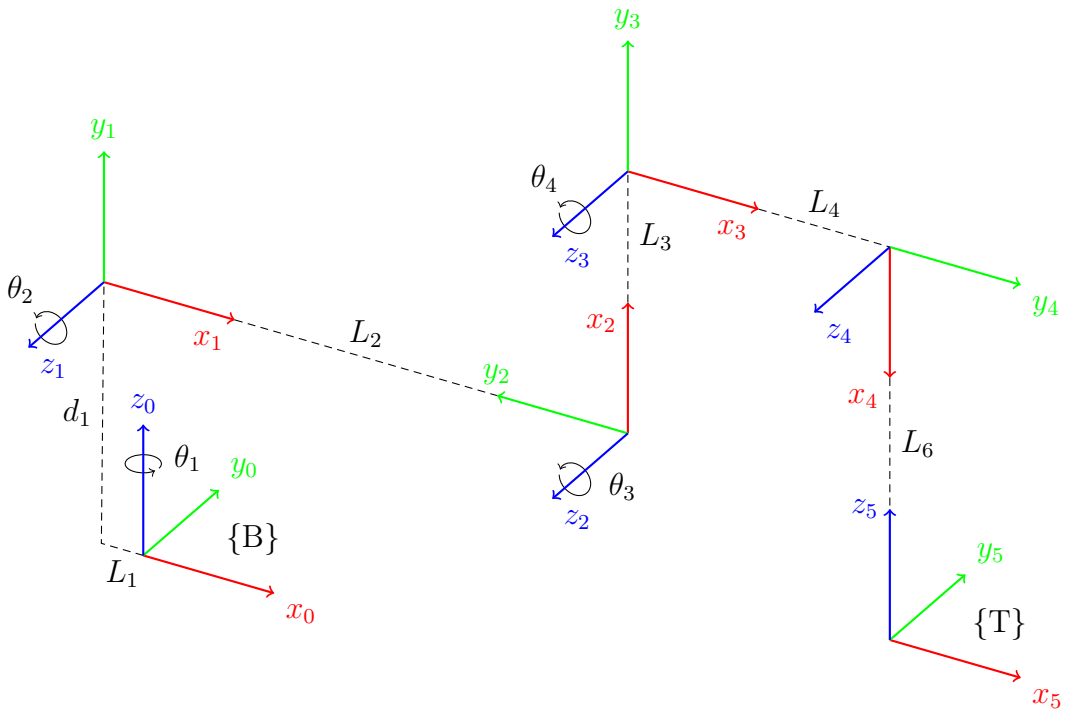

Figure 2.1 *Frame assignment for X88-540R.*

Three of the four DH parameters are always constants, which means each coordinate transform is a function of one joint variable – rotation θ_i in case of a revolute joint, or extension d_i in case of a prismatic joint. Based on these four parameters, coordinate transforms can be expressed with a standardized transformation matrix, which consists of a 3×3 rotation matrix for expressing change in orientation and a 3×1 translation vector for expressing change in location (see Eq. 2.1 below). [Sciavicco et al., 2000, p. 45]

$$\mathbf{T}_{i-1}^{i} = \begin{bmatrix} \cos(\theta_i) & -\sin(\theta_i)\cdot\cos(\alpha_i) & \sin(\theta_i)\cdot\sin(\alpha_i) & a_i\cdot\cos(\theta_i) \\ \sin(\theta_i) & \cos(\theta_i)\cdot\cos(\alpha_i) & -\cos(\theta_i)\cdot\sin(\alpha_i) & a_i\cdot\sin(\theta_i) \\ 0 & \sin(\alpha_i) & \cos(\alpha_i) & d_i \\ 0 & 0 & 0 & 1 \end{bmatrix} \tag{2.1}$$

The orientation and location of the end-effector frame {T} relative to a fixed base coordinate frame {B} can be expressed by means of matrix multiplication of the successive coordinate transforms as

$$\mathbf{T}_{\{B\}}^{\{T\}} = \mathbf{T}_0^1 \cdot \mathbf{T}_1^2 \cdot \mathbf{T}_2^3 \cdot \mathbf{T}_3^4 \cdot \mathbf{T}_4^5 \tag{2.2}$$

DH parameters corresponding to the assigned frames are presented in Table 2.1.

Table 2.1 *DH parameters for X88-540R. Joint variables denoted with an asterisk.*

i	$\boldsymbol{a}_i$	$\boldsymbol{\alpha}_i$	$\boldsymbol{d}_i$	$\boldsymbol{\theta}_i$
1	$-L_1$	$\frac{\pi}{2}$	d_1	θ_1^*
2	L_2	0	0	θ_2^*
3	L_3	0	0	θ_3^*
4	L_4	0	0	θ_4^*
5	L_6	$-\frac{\pi}{2}$	0	$\frac{\pi}{2}$

Elements $(1,4)$, $(2,4)$ and $(3,4)$ of the resulting transformation matrix $\mathbf{T}_{\{B\}}^{\{T\}}$ describe the location of the tool tip in operational space as

$$\begin{bmatrix} p_x \\ p_y \\ p_z \end{bmatrix} = \begin{bmatrix} \cos(\theta_1)\cdot\big(-L_1{+}L_2\cos(\theta_2)+L_3\cos(\theta_2+\theta_3)+L_4\cos(\theta_2+\theta_3+\theta_4)-L_6\sin(\theta_2+\theta_3+\theta_4)\big) \\ \sin(\theta_1)\cdot\big(-L_1{+}L_2\cos(\theta_2)+L_3\cos(\theta_2+\theta_3)+L_4\cos(\theta_2+\theta_3+\theta_4)-L_6\sin(\theta_2+\theta_3+\theta_4)\big) \\ d_1{+}L_2\sin(\theta_2)+L_3\sin(\theta_2+\theta_3)+L_4\sin(\theta_2+\theta_3+\theta_4)+L_6\cos(\theta_2+\theta_3+\theta_4) \end{bmatrix}$$

The mapping from cylinder stroke c_n to joint angle q_n is acquired from the law of cosines as

$$c_n = \sqrt{a_n^2 + b_n^2 - 2\cdot a_n\cdot b_n\cdot\cos(q_n)} \quad \Leftrightarrow \quad q_n = \cos^{-1}\left(\frac{c_n^2 - a_n^2 + b_n^2}{-2\cdot a_n\cdot b_n}\right) \tag{2.3}$$

The relation between cylinder extensions and DH angles is illustrated in Fig. 2.2.

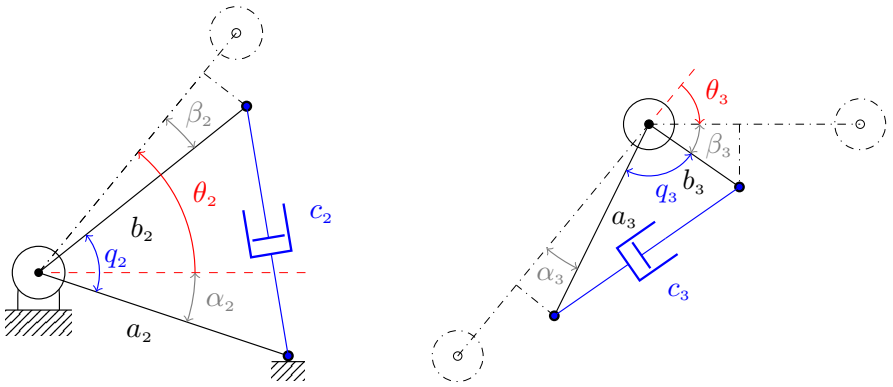

(a) Second cylinder and joint (b) Third cylinder and joint

Figure 2.2 *Relation between cylinder extensions and joint angles.*

$$q_2 = \theta_2 + \alpha_2 - \beta_2$$
$$q_3 = \theta_3 + \pi - \alpha_3 - \beta_3$$
$$q_4 = \theta_4 + \pi - \alpha_4 - \beta_4$$

2.1.1 Inverse kinematics of X88-540R

An algebraic solution technique exists for inverse kinematics of three-link planar arms [Sciavicco et al., 2000, p. 67–68]. The target orientation angle ϕ of the arm relative to the ground is defined as

$$\phi = \theta_2 + \theta_3 + \theta_4 \tag{2.4}$$

We can express the location of the fourth joint $(x_3,\, z_3)$ in two alternate ways:

$$\begin{cases} x_3 = p_x - L_4 \cdot \cos(\phi) = L_2 \cdot \cos(\theta_2) + L_3 \cdot \cos(\theta_2 + \theta_3) \\ z_3 = p_z - L_4 \cdot \sin(\phi) = L_2 \cdot \sin(\theta_2) + L_3 \cdot \sin(\theta_2 + \theta_3) \end{cases} \tag{2.5}$$

Squaring and summing the pair of equations yields

$$x_3^2 + z_3^2 = L_2^2 + L_3^2 + 2 \cdot L_2 \cdot L_3 \cdot \cos(\theta_3) \quad \Leftrightarrow \quad \cos(\theta_3) = \frac{x_3^2 + z_3^2 - L_2^2 - L_3^2}{2 \cdot L_2 \cdot L_3}$$

Applying the well-known trigonometric identity $\sin(x)^2 + \cos(x)^2 = 1$, we can solve for $\sin(\theta_3)$. In our case, only the solution in the so called elbow-up posture is

viable, so the solution candidate with a positive sign is neglected. Using the two-argument arctangent function (*atan2*) automatically handles placing the solution to the appropriate quadrant depending on the signs of the arguments. Now we have a solution for the third joint angle as

$$\theta_3 = \text{atan2}\left(\cos(\theta_3),\ -\sqrt{1-\cos^2(\theta_3)}\right)$$

Substituting θ_3 into the pair of equations 2.5 above, the unknowns $\sin(\theta_2)$ and $\cos(\theta_2)$ can be solved in a similar fashion as

$$\begin{cases} \cos(\theta_2) = \frac{x_3\cdot[L_2+L_3\cdot\cos(\theta_3)]+z_3\cdot L_3\cdot\sin(\theta_3)}{x_3^2+z_3^2} \\ \sin(\theta_2) = \frac{z_3\cdot[L_2+L_3\cdot\cos(\theta_3)]-x_3\cdot L_3\cdot\sin(\theta_3)}{x_3^2+z_3^2} \end{cases} \Rightarrow \theta_2 = \text{atan2}\left(\cos(\theta_2),\ \sin(\theta_2)\right)$$

Finally, the angle θ_4 that leads to the specified orientation ϕ of the arm can be solved from Eq. 2.4 as

$$\theta_4 = \phi - \theta_2 - \theta_3$$

The workspace of the arm in 90 degree tool orientation is illustrated in Fig. 2.3.

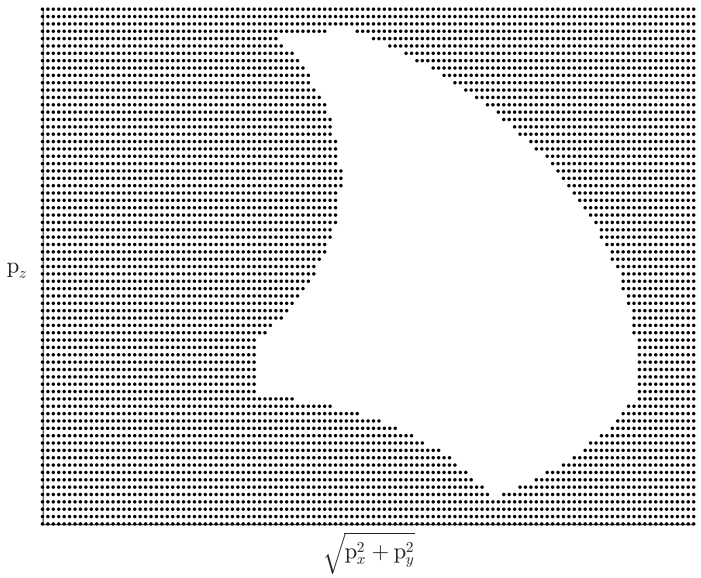

Figure 2.3 *Workspace of the planar arm in a vertical tool orientation.*

2.1.2 Differential kinematics of X88-540R

The end-effector Jacobian $\mathbf{J}_x$ relates angular joint velocities $\dot{\theta}$ to the Cartesian velocity $\dot{x}$ of the boom tip. It is derived by differentiating the end-effector location vector $[\ p_x\ p_y\ p_z\ ]^{\mathrm{T}}$ from the previously derived forward kinematic transformation

matrix, in terms of each joint variable. [Sciavicco et al., 2000, p. 101]

$$\dot{x} = \mathbf{J}_x(\theta) \cdot \dot{\theta} = \begin{bmatrix} \frac{\partial p_x}{\partial \theta_2} & \frac{\partial p_x}{\partial \theta_3} & \frac{\partial p_x}{\partial \theta_4} \\ \frac{\partial p_y}{\partial \theta_2} & \frac{\partial p_y}{\partial \theta_3} & \frac{\partial p_y}{\partial \theta_4} \\ \frac{\partial p_z}{\partial \theta_2} & \frac{\partial p_z}{\partial \theta_3} & \frac{\partial p_z}{\partial \theta_4} \end{bmatrix} \begin{bmatrix} \dot{\theta}_2 \\ \dot{\theta}_3 \\ \dot{\theta}_4 \end{bmatrix} \tag{2.6}$$

Angular acceleration can be solved from linear acceleration by differentiation with chain rule

$$\ddot{\theta} = \mathbf{J}_x^{-1}(\theta) \cdot \left(\ddot{x} - \dot{\mathbf{J}}_x(\theta) \cdot \dot{\theta} \right)$$

The relation between joint velocities and cylinder velocities is acquired by differentiating the previously derived mapping between cylinder extensions and joint angles.

$$\frac{\partial c_n}{\partial \theta_n} = \frac{\partial c_n}{\partial q_n} = \frac{-\frac{1}{2} \cdot 2 \cdot a_n \cdot b_n \cdot -sin(q_n)}{\sqrt{a_n^2 + b_n^2 - 2 \cdot a_n \cdot b_n \cdot cos(q_n)}} = \frac{a_n \cdot b_n \cdot \sin(q_n)}{c_n}$$

The actuator Jacobian $\mathbf{J}_c$ in this case is a diagonal matrix, since there is no coupling between cylinder velocities (i.e. no parallel structure is present in the manipulator).

$$\dot{c} = \mathbf{J}_c(\theta) \cdot \dot{\theta} = \begin{bmatrix} \frac{\partial c_2}{\partial \theta_2} & 0 & 0 \\ 0 & \frac{\partial c_3}{\partial \theta_3} & 0 \\ 0 & 0 & \frac{\partial c_4}{\partial \theta_4} \end{bmatrix} \begin{bmatrix} \dot{\theta}_2 \\ \dot{\theta}_3 \\ \dot{\theta}_4 \end{bmatrix} \tag{2.7}$$

Based on the principle of virtual work [Craig, 2005, p. 157], the Jacobian transpose can be used to map forces between actuator space, configuration space and operational space as

$$\tau = \mathbf{J}_x^{\mathrm{T}}(\theta) \cdot F_x$$
$$f_c = \mathbf{J}_c^{-\mathrm{T}}(\theta) \cdot \tau$$

where τ is the vector of joint torques, f_c is the vector of piston forces and F_x is the vector of forces in operational space. Combining all the results derived so far, we have the following relations between velocities and forces in actuator space and operational space:

$$\dot{x} = \mathbf{J}(\theta) \cdot \dot{c} = \left(\mathbf{J}_x(\theta) \cdot \mathbf{J}_c^{-1}(\theta) \right) \cdot \dot{c}$$
$$\dot{c} = \mathbf{J}^{-1}(\theta) \cdot \dot{x} = \left(\mathbf{J}_x^{-1}(\theta) \cdot \mathbf{J}_c(\theta) \right) \cdot \dot{x}$$
$$f_c = \mathbf{J}^{\mathrm{T}}(\theta) \cdot F_x = \left(\mathbf{J}_x^{\mathrm{T}}(\theta) \cdot \mathbf{J}_c^{-\mathrm{T}}(\theta) \right) \cdot F_x$$
$$F_x = \mathbf{J}^{-\mathrm{T}}(\theta) \cdot f_c = \left(\mathbf{J}_x^{-\mathrm{T}}(\theta) \cdot \mathbf{J}_c^{\mathrm{T}}(\theta) \right) \cdot f_c$$

2.2 Dynamic equation of the boom

For deriving the manipulator dynamics, the energy-based Euler-Lagrange formalism will be followed. It is often preferred due to its intuitive and systematic nature, although computationally inefficient for manipulators with increasing complexity, which has motivated the development of the subsystem-based control known as virtual decomposition control, relying on the alternative recursive Newton-Euler method [De Schutter et al., 1997, p. 12]. The closed-form equations acquired from Lagrange's equations represent an ideal serial manipulator and lack some precision since they do not model cylinder mechanics separately.

The general dynamic equation of manipulators in configuration-space assumes the form

$$\tau = \mathbf{I}(\theta) \cdot \ddot{\theta} + \cancel{\mathbf{C}(\theta, \dot{\theta})} + \mathbf{G}(\theta) + \tau_{ext} \ ,$$

where $\mathbf{I}(\theta)$ is the configuration-dependent matrix of inertial terms, $\mathbf{G}(\theta)$ is the configuration-dependent vector of gravity torques and τ_{ext} is the vector of external torques affecting to the manipulator. Assuming small operating velocities, Coriolis and centrifugal terms $\mathbf{C}(\theta, \dot{\theta})$ can be neglected to simplify the dynamic equation.

Only two-dimensional dynamics along the plane formed by the arm joints (namely *lift*, *tilt* and *breaker*) will be considered in this thesis. The Langrangian $\mathcal{L}$ of the system is defined as

$$\mathcal{L} = \mathcal{K}(\theta, \dot{\theta}) - \mathcal{P}(\theta) \ , \tag{2.8}$$

where $\mathcal{K}$ and $\mathcal{P}$ denote total kinetic and potential energies of the manipulator, respectively. The required driving torque for the n:th joint can be calculated from

$$\tau_n = \frac{d}{dt}\left(\frac{\partial \mathcal{L}}{\partial \dot{\theta}_n}\right) - \frac{\partial \mathcal{L}}{\partial \theta_n} = \frac{d}{dt}\left(\frac{\partial \mathcal{K}}{\partial \dot{\theta}_n}\right) - \left(\frac{\partial \mathcal{K}}{\partial \theta_n} - \frac{\partial \mathcal{P}}{\partial \theta_n}\right) \tag{2.9}$$

For this purpose, one has to calculate the global velocities (i.e. the velocity with respect to the base) of each point mass m_n, by deriving the centre-of-mass (COM) Jacobian $\mathbf{J}_{m_n}$ with respect to the configuration-dependent location $\overline{p}_{m_n}$ of each link mass. [Jazar, 2010, p. 620–625]

$$\overline{p}_{m_n}(\theta) = \begin{bmatrix} x_{m_n} \\ z_{m_n} \end{bmatrix} \quad \Rightarrow \quad \mathbf{J}_{m_n}(\theta) = \begin{bmatrix} \frac{\partial x_{m_n}}{\partial \theta_2} & \frac{\partial x_{m_n}}{\partial \theta_3} & \frac{\partial x_{m_n}}{\partial \theta_4} \\ \frac{\partial z_{m_n}}{\partial \theta_2} & \frac{\partial z_{m_n}}{\partial \theta_3} & \frac{\partial z_{m_n}}{\partial \theta_4} \end{bmatrix} \tag{2.10}$$

Locations of each COM from the driving joint along the link are r_2, r_3 and r_4.

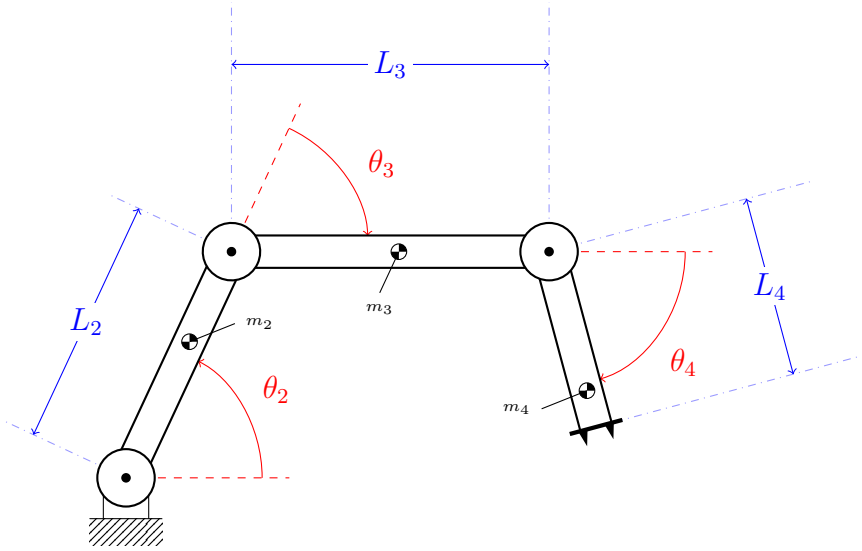

Figure 2.4 *DH angles and link masses illustrated. Note that* $\theta_3 < 0$ *and* $\theta_4 < 0$.

Total potential energy $\mathcal{P}$ of the planar arm is calculated as

$$\mathcal{P} = -\sum_{i=2}^{4} \left(m_i \cdot \overline{g}_0^{\mathrm{T}} \cdot \overline{p}_{m_i} \right) = \sum_{i=2}^{4} \left(m_i \cdot g \cdot z_{m_i} \right) , \tag{2.11}$$

where $\overline{g}_0$ is the gravity acceleration vector, in this particular case $\overline{g}_0^{\mathrm{T}} = [\ 0\ -g\ ]$, since gravity affects in the direction of the base Z-axis [Sciavicco et al., 2000, p. 139–140]. The gravitational torque $\tau_{gravity,n}$ affecting link n can be calculated from the equation

$$\tau_{gravity,n} = \frac{\partial \mathcal{P}}{\partial \theta_n} = -\sum_{i=n}^{4} \left(m_i \cdot \overline{g}_0^{\mathrm{T}} \cdot \mathbf{J}_{m_i} \dot{\theta} \right) = \sum_{i=n}^{4} \left(m_i \cdot g \cdot \dot{z}_{m_i} \right) \tag{2.12}$$

The calculations for gravity torques resulting from the previous equation are presented below.

$$\tau_{gravity,4} = \mathrm{m}_4 \cdot g \cdot r_4 \cdot \cos(\theta_2 + \theta_3 + \theta_4)$$

$$\tau_{gravity,3} = \tau_{gravity,4} + \mathrm{m}_4 \cdot g \cdot L_3 \cdot \cos(\theta_2 + \theta_3) + \mathrm{m}_3 \cdot g \cdot r_3 \cdot \cos(\theta_2 + \theta_3)$$

$$\tau_{gravity,2} = \tau_{gravity,3} + (\mathrm{m}_4 + \mathrm{m}_3) \cdot g \cdot L_2 \cdot \cos(\theta_2) + \mathrm{m}_2 \cdot g \cdot r_2 \cdot \cos(\theta_2)$$

The configuration-dependent gravity vector $\mathbf{G}(\theta)$ is written as

$$\mathbf{G}(\theta) = \begin{bmatrix} \mathrm{m}_4 \cdot g \cdot [\, r_4 \cdot \cos(\theta_2+\theta_3+\theta_4) + L_3 \cdot \cos(\theta_2+\theta_3) + L_2 \cdot \cos(\theta_2) \,] \\ + \,\mathrm{m}_3 \cdot g \cdot [\, r_3 \cdot \cos(\theta_2+\theta_3) + L_2 \cdot \cos(\theta_2) \,] + \mathrm{m}_2 \cdot g \cdot r_2 \cdot \cos(\theta_2) \\ \\ \mathrm{m}_4 \cdot g \cdot [\, r_4 \cdot \cos(\theta_2+\theta_3+\theta_4) + L_3 \cdot \cos(\theta_2+\theta_3) \,] + \mathrm{m}_3 \cdot g \cdot r_3 \cdot \cos(\theta_2+\theta_3) \\ \\ \mathrm{m}_4 \cdot g \cdot r_4 \cdot \cos(\theta_2+\theta_3+\theta_4) \end{bmatrix}$$

Rotational and translational kinetic energy $\mathcal{K}$ of the planar arm is

$$\begin{aligned} \mathcal{K} &= \sum_{i=2}^{4} \left(\tfrac{1}{2} \cdot I_i \cdot \dot{\theta}_i^2 + \tfrac{1}{2} \cdot m_i \cdot (\mathbf{J}_{m_i}\dot{\theta})^{\mathrm{T}} \cdot (\mathbf{J}_{m_i}\dot{\theta}) \right) \\ &= \sum_{i=2}^{4} \left(\tfrac{1}{2} \cdot I_i \cdot \dot{\theta}_i^2 + \tfrac{1}{2} \cdot m_i \cdot (\dot{x}_{m_i}^2 + \dot{z}_{m_i}^2) \right) \end{aligned}$$

where I_i is the moment of inertia of the i:th link along its axis of rotation. The inertial torque $\tau_{inertia,n}$ affecting link n can be calculated from the equation

$$\tau_{inertia,n} = \frac{d}{dt}\left(\frac{\partial \mathcal{K}}{\partial \dot{\theta}_n}\right) \quad \Rightarrow \quad \begin{bmatrix} \tau_{inertia,2} \\ \tau_{inertia,3} \\ \tau_{inertia,4} \end{bmatrix} = \mathbf{I}(\theta) \cdot \ddot{\theta} + \cancel{\dot{\mathbf{I}}(\theta) \cdot \dot{\theta}} \ ,$$

and can also be expressed in matrix form, where $\mathbf{I}(\theta)$ is referred to as the robot inertia matrix [Lewis et al., 1993, p. 76]. As mentioned before, only acceleration-dependent terms will be taken into account, while velocity-dependent terms are neglected. The inertial torques resulting from the previous equation are presented below.

$$\begin{aligned} \tau_{inertia,4} = {} & [\, I_4 + \mathrm{m}_4 \cdot r_4^2 \,] \cdot (\ddot{\theta}_2 + \ddot{\theta}_3 + \ddot{\theta}_4) \\ & + [\, \mathrm{m}_4 \cdot r_4 \cdot L_2 \cdot \cos(\theta_3+\theta_4) \,] \cdot \ddot{\theta}_2 + [\, \mathrm{m}_4 \cdot r_4 \cdot L_3 \cdot \cos(\theta_4) \,] \cdot (\ddot{\theta}_2 + \ddot{\theta}_3) \end{aligned}$$

$$\begin{aligned} \tau_{inertia,3} = {} & \tau_{inertia,4} + [\, I_3 + \mathrm{m}_3 \cdot r_3^2 + \mathrm{m}_4 \cdot L_3^2 \,] \cdot (\ddot{\theta}_2 + \ddot{\theta}_3) \\ & + [\, \mathrm{m}_3 \cdot r_3 \cdot L_2 \cdot \cos(\theta_3) \,] \cdot \ddot{\theta}_2 + [\, \mathrm{m}_4 \cdot L_2 \cdot L_3 \cdot \cos(\theta_3) \,] \cdot \ddot{\theta}_2 \\ & + [\, \mathrm{m}_4 \cdot r_4 \cdot L_3 \cdot \cos(\theta_4) \,] \cdot (\ddot{\theta}_2 + \ddot{\theta}_3 + \ddot{\theta}_4) \end{aligned}$$

$$\begin{aligned} \tau_{inertia,2} = {} & \tau_{inertia,3} + [\, I_2 + \mathrm{m}_2 \cdot r_2^2 + (\mathrm{m}_4 + \mathrm{m}_3) \cdot L_2^2 \,] \cdot \ddot{\theta}_2 \\ & + [\, \mathrm{m}_3 \cdot r_3 \cdot L_2 \cdot \cos(\theta_3) \,] \cdot (\ddot{\theta}_2 + \ddot{\theta}_3) + [\, \mathrm{m}_4 \cdot L_2 \cdot L_3 \cdot \cos(\theta_3) \,] \cdot (\ddot{\theta}_2 + \ddot{\theta}_3) \\ & + [\, \mathrm{m}_4 \cdot r_4 \cdot L_2 \cdot \cos(\theta_3+\theta_4) \,] \cdot (\ddot{\theta}_2 + \ddot{\theta}_3 + \ddot{\theta}_4) \end{aligned}$$

The inertia matrix of the three-link planar arm is written as

$$\mathbf{I}(\theta) = \begin{bmatrix} \mathrm{M}_{22} & \mathrm{M}_{23} & \mathrm{M}_{24} \\ \mathrm{M}_{32} & \mathrm{M}_{33} & \mathrm{M}_{34} \\ \mathrm{M}_{42} & \mathrm{M}_{43} & \mathrm{M}_{44} \end{bmatrix} ,$$

where

$$\begin{aligned} \mathrm{M}_{22} = (I_4 + \mathrm{m}_4\, r_4^2) + (I_3 + \mathrm{m}_3\, r_3^2 + \mathrm{m}_4\, L_3^2) + (I_2 + \mathrm{m}_2\, r_2^2 + \mathrm{m}_3\, L_2^2 + \mathrm{m}_4\, L_2^2) \\ + 2\,\mathrm{m}_4\, L_2\, r_4\, \cos(\theta_3 + \theta_4) + 2\,\mathrm{m}_4\, L_2\, L_3\, \cos(\theta_3) \\ + 2\,\mathrm{m}_3\, L_2\, r_3\, \cos(\theta_3) + 2\,\mathrm{m}_4\, L_3\, r_4\, \cos(\theta_4) \end{aligned}$$

$$\begin{aligned} \mathrm{M}_{23} = \mathrm{M}_{32} = (I_4 + \mathrm{m}_4\, r_4^2) + (I_3 + \mathrm{m}_3\, r_3^2 + \mathrm{m}_4\, L_3^2) + \mathrm{m}_4\, L_2\, L_3\, \cos(\theta_3) \\ + 2\,\mathrm{m}_4\, L_3\, r_4\, \cos(\theta_4) + \mathrm{m}_3\, L_2\, r_3\, \cos(\theta_3) + \mathrm{m}_4\, L_2\, r_4\, \cos(\theta_3 + \theta_4) \end{aligned}$$

$$\mathrm{M}_{24} = \mathrm{M}_{42} = (I_4 + \mathrm{m}_4\, r_4^2) + \mathrm{m}_4\, L_2\, r_4\, \cos(\theta_3 + \theta_4) + \mathrm{m}_4\, L_3\, r_4\, \cos(\theta_4)$$

$$\mathrm{M}_{33} = (I_4 + \mathrm{m}_4\, r_4^2) + (I_3 + \mathrm{m}_3\, r_3^2 + \mathrm{m}_4\, L_3^2) + 2\,\mathrm{m}_4\, L_3\, r_4\, \cos(\theta_4)$$

$$\mathrm{M}_{34} = \mathrm{M}_{43} = (I_4 + \mathrm{m}_4\, r_4^2) + \mathrm{m}_4\, L_3\, r_4\, \cos(\theta_4)$$

$$\mathrm{M}_{44} = I_4 + \mathrm{m}_4\, r_4^2$$

Matlab-code of the inverse dynamics including Coriolis and centrifugal terms is provided in Appendix A. The dynamic equations were verified using a *Simscape Multibody* –model of the boom forward dynamics as a reference and seem to catch the essence of the dynamic behaviour of the boom, as can be seen from Figure 2.5.

However, the parameters acquired from geometric models are not accurate and do not take friction into account, which is why the dynamic parameters should be identified experimentally. Linear parametrization of the dynamic equation is achieved by separating inverse dynamics into the form

$$\tau = \mathbf{I}(\theta) \cdot \ddot{\theta} + \mathbf{G}(\theta) + \mathbf{J}_c^{\mathrm{T}} \cdot \mathcal{F}(\dot{c}) = \mathbf{Y}(\ddot{\theta}, \dot{\theta}, \theta) \cdot \varphi \ , \tag{2.13}$$

where $\mathbf{Y}$ is the regressor matrix, φ is the parameter vector and $\mathcal{F}$ is a model of cylinder friction [Lewis et al., 1993, p. 89].

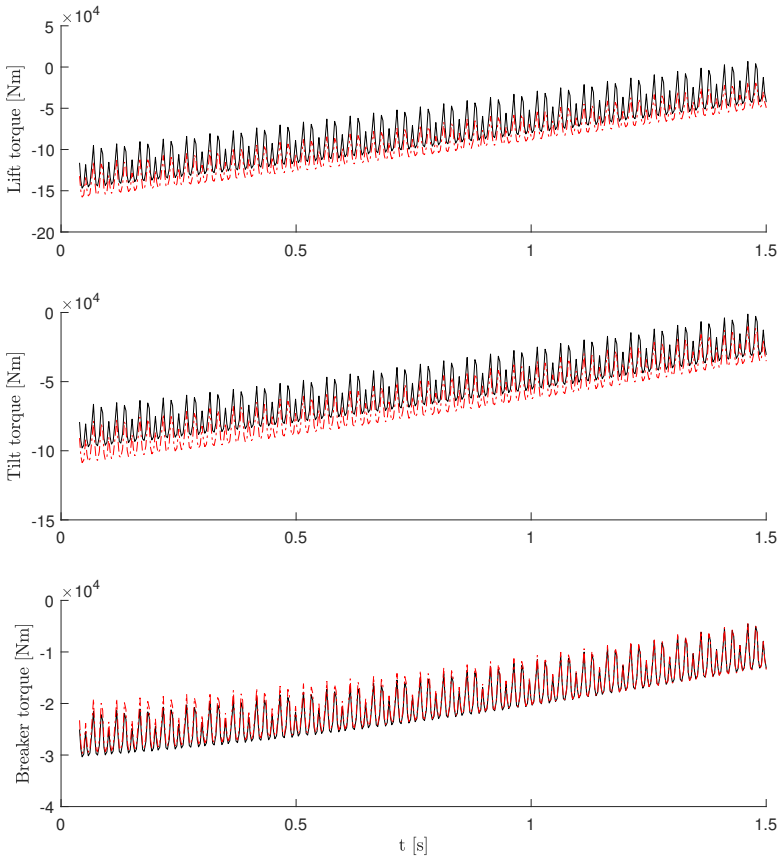

Figure 2.5 *Inverse dynamics (black line) compared to model (dashed red line).*

A difference of joint torques in the form $\tau_i - \tau_{i+1}$ can be used instead of the absolute value of measured joint torques, which results in better numerical precision than using the coupled equations, since the regression matrix has more zero-valued elements [Tafazoli, 1997, p. 110]. The matrix $\mathbf{Y_d}$ below is the inertial and gravitational part of the regressor matrix and φ_d its parameter vector.

$$\begin{bmatrix} \tau_2 - \tau_3 \\ \tau_3 - \tau_4 \\ \tau_4 \end{bmatrix} = \underbrace{\mathbf{Y_d}(\theta, \dot{\theta}, \ddot{\theta})}_{\in\, \mathbb{R}^{3\times 6}} \cdot \underbrace{\varphi_d}_{\in\, \mathbb{R}^6}$$

$$= \begin{bmatrix} \ddot{\theta}_2 & 0 & 0 & g\cdot\cos(\theta_2) & L_2\cdot\cos(\theta_3)\cdot(\ddot{\theta}_2+\ddot{\theta}_3) & L_2\cdot\cos(\theta_3+\theta_4)\cdot(\ddot{\theta}_2+\ddot{\theta}_3+\ddot{\theta}_4) \\ 0 & \ddot{\theta}_2+\ddot{\theta}_3 & 0 & 0 & L_2\cdot\cos(\theta_3)\cdot\ddot{\theta}_2 + g\cdot\cos(\theta_2+\theta_3) & L_3\cdot\cos(\theta_4)\cdot(\ddot{\theta}_2+\ddot{\theta}_3+\ddot{\theta}_4) \\ 0 & 0 & \ddot{\theta}_2+\ddot{\theta}_3+\ddot{\theta}_4 & 0 & 0 & \begin{array}{l} L_2\cdot\cos(\theta_3+\theta_4)\cdot\ddot{\theta}_2 \\ +L_3\cdot\cos(\theta_4)\cdot(\ddot{\theta}_2+\ddot{\theta}_3) \\ +g\cdot\cos(\theta_2+\theta_3+\theta_4) \end{array} \end{bmatrix}$$

$$\times \begin{bmatrix} I_2 + m_2\cdot r_2^2 + (m_3+m_4)\cdot L_2^2 \\ I_3 + m_3\cdot r_3^2 + m_4\cdot L_3^2 \\ I_4 + m_4\cdot r_4^2 \\ m_2\cdot r_2 + (m_3+m_4)\cdot L_2 \\ m_3\cdot r_3 + m_4\cdot L_3 \\ m_4\cdot r_4 \end{bmatrix}$$

If only sliding friction is considered including static friction and viscous friction terms, the frictional part of the regressor matrix $\mathbf{Y_f}$ and its parameter vector φ_f can be expressed as

$$\mathbf{J}_c^{\mathrm{T}} \cdot \underbrace{\mathbf{Y_f}(\dot{c})}_{\in\, \mathbb{R}^{3\times 6}} \cdot \underbrace{\varphi_f}_{\in\, \mathbb{R}^{6}}$$

$$= \mathbf{J}_c^{\mathrm{T}} \cdot \begin{bmatrix} \operatorname{sgn}(\dot{c}_2) & \dot{c}_2 & -\operatorname{sgn}(\dot{c}_3) & -\dot{c}_3 & 0 & 0 \\ 0 & 0 & \operatorname{sgn}(\dot{c}_3) & \dot{c}_3 & -\operatorname{sgn}(\dot{c}_4) & -\dot{c}_4 \\ 0 & 0 & 0 & 0 & \operatorname{sgn}(\dot{c}_4) & \dot{c}_4 \end{bmatrix} \begin{bmatrix} f_{s2} \\ f_{v2} \\ f_{s3} \\ f_{v3} \\ f_{s4} \\ f_{v4} \end{bmatrix}$$

Notice how friction of the distal link is substracted in the torque difference form, since friction is a local phenomenon in each actuator and does not affect the load pressure of the adjacent link. For asymmetric cylinders, two different friction coefficients (f_s for static friction and f_v for viscous friction) could be separately identified for extension and retraction movements to increase accuracy.

3. IMPEDANCE SHAPING CONTROL

Contact forces between the manipulator and an environment impose constraints on the motion of the manipulator, which introduces conflicting goals between position and force control objectives. Position-controlled manipulators treat contact with the environment as a disturbance and try to satisfy commanded position goals at all costs, leading to excessive force buildup that could possibly damage the manipulator [Craig, 2005, p. 13]. Exchange of mechanical work between the manipulator and the environment equals the product of force and velocity – if exchange of energy between the systems is not negligible, controlling only one power variable (i.e. explicit force control or pure motion control) might not suffice to guarantee stable interaction between the two systems [Craig, 2005, p. 317].

Therefore, in order to successfully execute contact tasks, the ability of robots to comply with their surroundings becomes a critical issue. Traditionally, this matter has been dealt with by increasing the intrisic compliance of robots with additional hardware – passive compliance devices, such as spring elements attached to the end-effector [Craig, 2005, p. 333]. A more novel approach to the problem of compliant manipulation is to accommodate the manipulator to external forces based on sensory information, which is referred to as active compliance and is illustrated in Fig. 3.1.

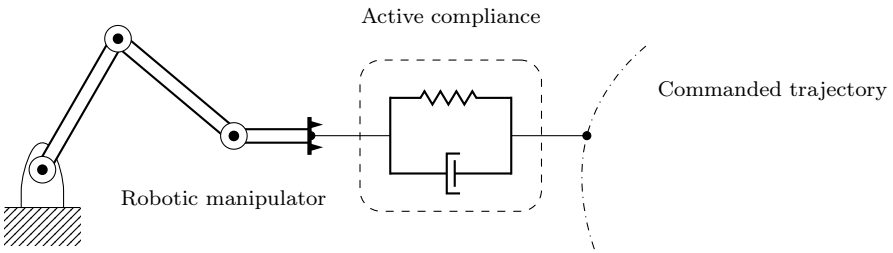

Figure 3.1 *Active compliance in the form of programmable stiffness and viscosity.*

This has motivated an approach to manipulation known as impedance control, which aims at controlling port behaviour – impedance or admittance – rather than either of the power variables explicitly. Mechanical impedance Z is a dynamic relation which generates force as a function of motion, while mechanical admittance relates

motion to force. Impedance and admittance can describe arbitrarily complex dynamic behavior, but are most often adopted in the second-order form, consisting of damping (i.e. resistance to change of velocity) and inertia (i.e. resistance to change of acceleration) in addition to stiffness [Buerger and Hogan, 2005, p. 6].

$$Z = \frac{F}{x}$$

An impedance controller acts to minimize deviations from a reference target model, which specifies the desired dynamic response of the manipulator when interacting with the environment. Impedance controllers effectively attempt to mask the impedance of the manipulator by introducing a virtual bumper to its end-effector, mimicking the behaviour of a mass-spring-damper system (see Fig 3.2) with arbitrarily chosen inertia, damping and stiffness. The range of achievable impedances is limited by the physical capabilities of the manipulator and the bandwidth of its control system, which is why the target model is only realizable over some limited frequency range.

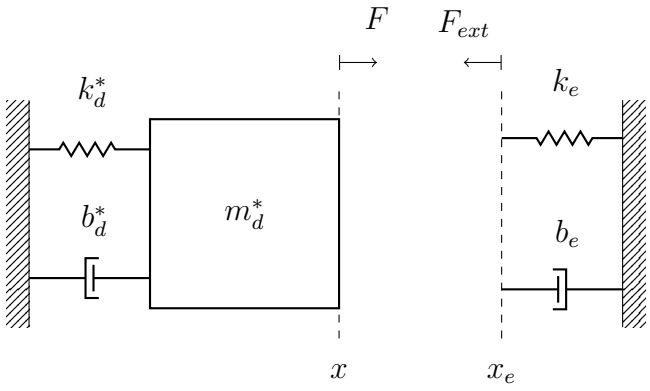

Figure 3.2 *1-DOF example of a mechanism interacting with an environment. Characteristics of a stiff contact surface can be modeled as a spring-damper without inertia.*

Target impedance specifies the objective dynamics by establishing a dynamical relationship between contact force and position deviation, e.g. by creating a motion response to a sensed contact force, which alters the trajectory of the manipulator. Target impedance is most often adopted in the form of a linear time-invariant mass-spring-damper system to facilitate control design, in which case the impedance is the algebraic inverse of admittance and vice versa. The second-order impedance is expressed as

$$F_{ext} = m_d \cdot (\ddot{x}_0 - \ddot{x}) + b_d \cdot (\dot{x}_0 - \dot{x}) + k_d \cdot (x_0 - x) \ , \tag{3.1}$$

where F_{ext} is the sensed contact force, m_d the desired inertia, b_d the desired damping and k_d the desired stiffness. The desired values for inertia, damping and stiffness are collectively referred to as impedance parameters. [Vukobratovic et al., 2009, p. 18]

Since impedance control regulates the relationship between force and motion, it does not explicitly control force or motion, but instead these two power variables are implicitly determined by the desired port behaviour. Impedance control falls into the category of indirect force control, which means achieving force control by means of motion control. It differs from other interaction control schemes – namely hybrid and parallel control, which both are forms of explicit force control – in it's motion constraint paradigm, by establishing dynamic constraints rather than geometric constraints [De Schutter et al., 1997, p. 7]. The recognized advantages of impedance control compared to pure motion control or explicit force control include achieving inherent robustness with respect to uncertain environments. Moreover, compliance by software allows the impedance parameters to be varied programmatically on the fly, making the manipulator more versatile with regard to different types of environments and allowing adaptive and learning strategies to be employed.

A drawback of impedance control is the need for more complex and expensive additional hardware due to force and torque sensing requirements, although the contact force could be estimated by means of observers, and in hydraulic systems pressure-based force sensing is relatively cost-effective. Compared to passive compliance devices which have energy storage capability and effectively unlimited bandwidth, an active compliance controller has limited bandwidth, consumes energy in achieving compliant behaviour and cannot store energy in its actuation system. Therefore it cannot absord shocks except for a limited range of frequencies, yet on the other hand, there are no risks related to the sudden and uncontrollable release of energy stored in springs [Boaventura et al., 2015]. Finally, the absence of a general framework for the synthesis of controller parameters that would ensure stability and performance makes the control design process unsystematic [Vukobratovic et al., 2009, p. 65].

3.1 Cascaded compliance control

Cascaded compliance control, or inner/outer loop impedance control, is based on nested position and force feedback loops. The manipulator and its environment are represented as impedances and admittances – if the manipulator assumes the form of an impedance, the environment will assume the form of an admittance and vice versa. Thereby two alternative implementations of cascaded impedance control can be distinguished, depending in which manner the feedback loops are nested – the

manipulator can be either a motion source or a force source, and respectively the controller will be an admittance or an impedance. In case of a position-controlled manipulator, the controller assumes the form of an admittance and the control scheme is referred to as position-based impedance control (PBIC), or admittance control. [Ott et al., 2015]

Alternatively, if the manipulator is force-controlled, the control scheme is known as force-based impedance control (FBIC) or explicit impedance control, since the controller modulates impedance. FBIC is based on an inner force feedback loop and an outer motion feedback loop, where the inner loop complies the manipulator while the outer loop stiffens the manipulator (see Fig. 3.3). In other words, an explicit impedance controller stiffens the force command of a soft force source, and acceleration and velocity feedbacks are required in addition to position feedback.

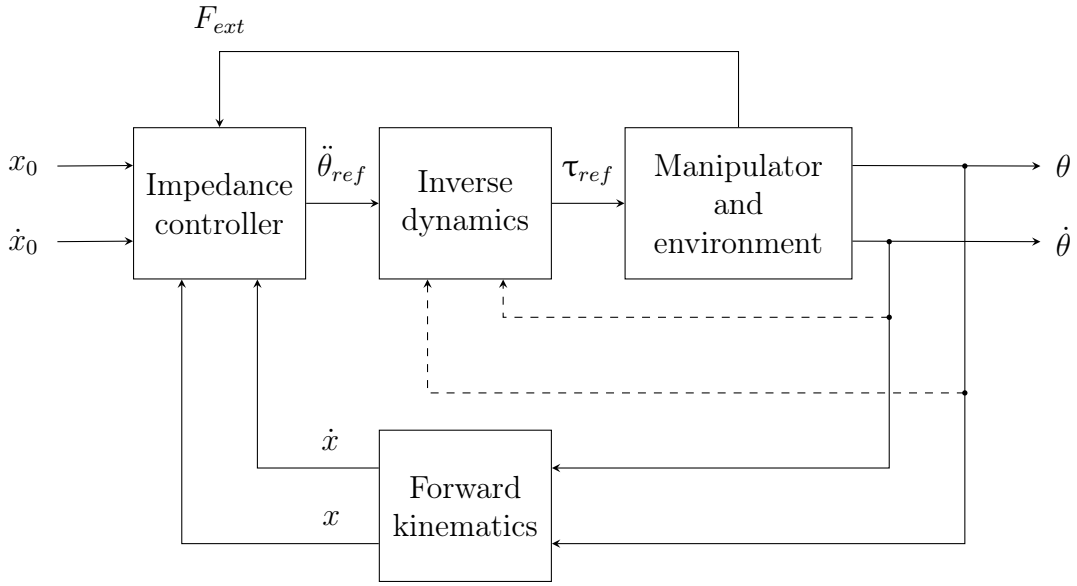

Figure 3.3 *Force-based impedance control. [Boaventura et al., 2015]*

The force control loop is active even in free-space motion, which is why FBIC suffers from poor position control performance in free-space, due to unmodeled dynamics such as friction [Muhammad et al., 2009]. Therefore FBIC would inevitably require a switching law to transition from stiff position control to impedance regulation, when contact with the environment is detected. Force control of hydraulic actuators is a strongly nonlinear and therefore challenging problem, adding to the inconvenience of implementing a force-based impedance controller.

Choosing on causality between impedance and admittance depends strongly on the properties of the manipulator and nature of the task. Most environments of interest act as rigid kinematic contraints with nearly infinite impedance, which can only be

represented as an admittance – an argument for making the manipulator behave as an impedance source. But since in most cases the inertial properties of the manipulator dominate its response, in practice it is more feasible to make the manipulator appear as an admittance. [Buerger and Hogan, 2005, p. 10]

3.1.1 Position-based impedance control

In contrast to FBIC, only position feedback is needed to implement PBIC, which makes it attractive since acceleration and velocity information is often either of poor quality or not available at all. PBIC allows exploiting readily existing position controllers without significant modifications, which makes it a more generally applicable control scheme in industrial robotics. The majority of commercially available manipulators are designed as positioning devices and do not allow receiving force or torque commands directly. [Vukobratovic et al., 2009, p. 262]

PBIC is based on an inner position feedback loop nested inside an outer force feedback loop – the inner loop stiffens the manipulator and the outer loop complies the manipulator, so the target admittance filter effectively softens the position command of a stiff position source. The outer force-feedback loop is depicted in Fig. 3.4 and the inner position-feedback loop is depicted in Fig. 3.5.

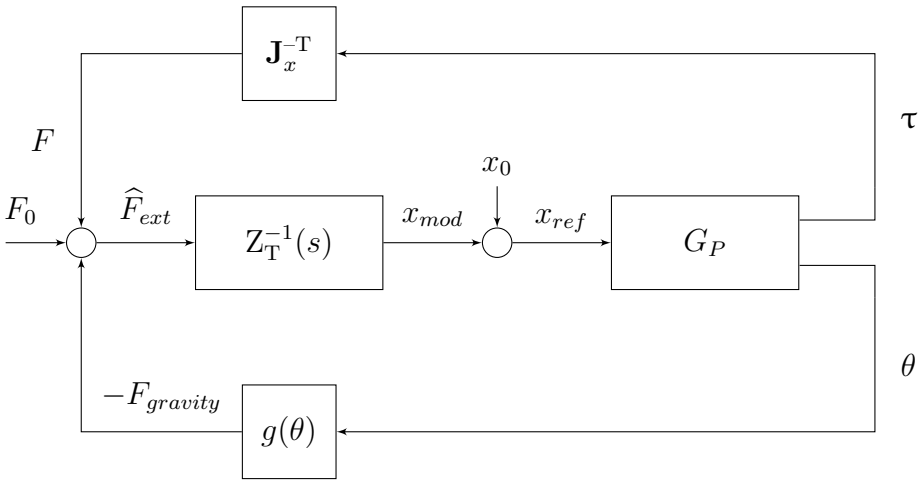

Figure 3.4 *Block diagram of the outer Cartesian force control loop. G_P signifies the position-controlled plant, $\mathrm{Z}_\mathrm{T}^{-1}$ the target impedance filter and $g(\theta)$ gravity compensation.*

In free-space motion, assuming inertial and gravitational forces are fully compensated, the sensed external contact force $\widehat{F}_{ext}$ and the position modification x_{mod} are close to zero and the outer force control loop is effectively passive. In such a case position reference x_{ref} equals nominal position reference x_0. The nominal reference

should only be reached when in unconstrained motion, when no external contact forces are acting on the manipulator.

The outer force feedback loop closes naturally when contact occurs and the feedback compensator Z_T^{-1} creates a position adjustment corresponding to the sensed external forces, leading to a modified position reference which differs from the nominal position reference. The feedback compensator used to regulate impedance or admittance is generally referred to as the target impedance filter. The impedance filter Z_T^{-1} modifies the position reference based on the sensed contact forces, according to the equation

$$x_{ref} = x_0 + x_{mod} = x_0 + Z_T^{-1} \cdot \widehat{F}_{ext}$$

The purpose of the modified position reference is to indirectly regulate the contact force imposed by the manipulator to the environment, by locating the reference trajectory of the end-effector within the object. While this modified position reference is not supposed to be reached by the manipulator, it is nevertheless useful in regulating the force applied to the environment. The modified position reference does not necessarily need to be realizable nor even inside the workspace of the manipulator.

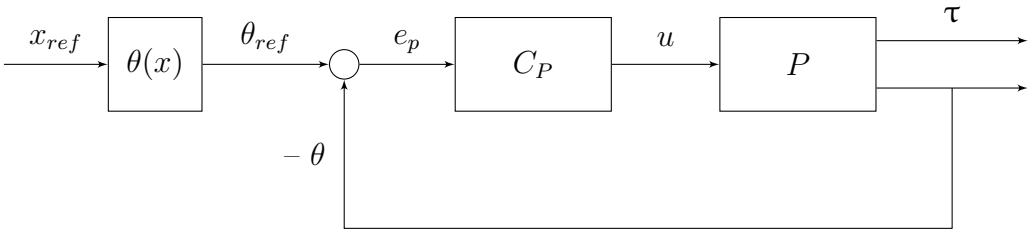

Figure 3.5 *Block diagram of the inner joint position control loop.*

The impedance filter implements low-pass filtering behaviour with a small cutoff frequency [Vukobratovic et al., 2009, p. 410]. It can be expressed in the Laplace-domain as

$$Z_T^{-1}(s) = \frac{X(s)}{F(s)} = \frac{1}{m_d \cdot s^2 + b_d \cdot s + k_d} \ , \tag{3.2}$$

from which we can see that admittance, unlike impedance, has the advantage of being a proper rational function.

3.1.2 Performance/robustness -tradeoff

In feedback-based impedance control, a tradeoff exists between impedance tracking accuracy and stability in face of changing environments. Due to a lower sampling

frequency, the outer loop is more limited in its ability to change system behaviour than the inner loop, as the outer loop rolls off at higher frequencies and is unable to modify the inherent dynamics of the plant [Colgate, 1989].

This means PBIC in general provides an excessively stiff response and suffers from an inability to provide very soft impedances with low values of stiffness and damping, making it prone to instability when facing rigid environments that require the manipulator to be highly compliant. In contrast, FBIC provides a too soft response and therefore suffers from an inability to provide very large impedances when making contact with elastic environments. This complementary nature of PBIC and FBIC with regard to performance and robustness is illustrated in Fig. 3.6.

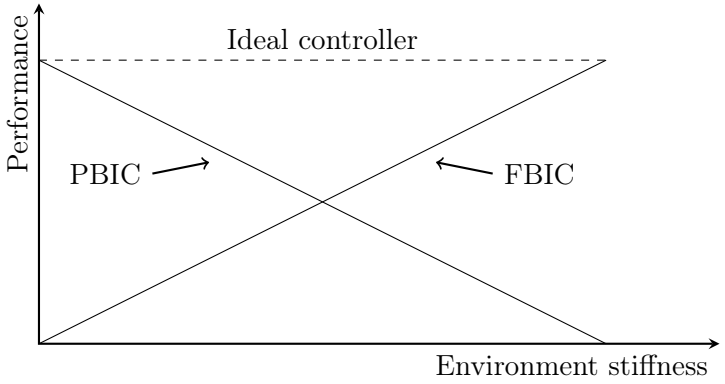

Figure 3.6 *Characteristics of PBIC and FBIC, after [Ott et al., 2015].*

This tradeoff between performance and robustness is due to feedback controllers introducing their own impedance to the system, which leads to unideally realized impedance. The effects of feedback-induced impedance errors can be separated into the inherent mechanical impedance of the inner feedback controller, which is dominant at high frequencies, and the mechanical impedance introduced by the target model, which is dominant at low frequencies [Colgate, 1989].

Because the actuators are never ideal motion or force sources, the inner feedback controller introduces its own impedance to the system. In PBIC, whenever the actual position of the manipulator differs from the desired one, the position controller introduces its own impedance to the system. This inherent impedance of the position controller is determined by its control gains, which are typically tuned in a way to minimize positioning errors in free-space motion – not in order to achieve best possible impedance tracking performance when in contact. This leads to a conflict in achieving positioning accuracy requirements in free-space and impedance tracking requirements in contact regime. [Valency and Zacksenhouse, 2003]

To illustrate the sources of impedance errors, the impedance error in PBIC is written as

$$e_p = x_0 - x = \frac{1}{1 + C_P \cdot P} \cdot x_0 + \frac{P}{1 + C_P \cdot P} \cdot F_{ext} + \frac{C_P \cdot P}{1 + C_P \cdot P} \cdot Z_T^{-1} \cdot F_{ext} \ ,$$

where the first two terms describe the free-space dynamics, including load dynamics, and the last term describes the target model realization error. We can define from Fig. 3.5 $G_P = \frac{C_P \cdot P}{1 + C_P \cdot P}$ as the closed-loop transfer function of the position-controlled plant and $S_P = \frac{1}{1 + C_P \cdot P}$ as its sensivity function. [Vukobratovic et al., 2009, p. 267]

The position of the manipulator is then written as

$$x = G_P \cdot (x_0 - Z_T^{-1} \cdot F_{ext}) + S_P \cdot P \cdot F_{ext} \ ,$$

and the realized closed-loop admittance equals to

$$\frac{x}{F_{ext}} = G_P \cdot Z_T^{-1} + S_P \cdot P \ ,$$

which would equal to Z_T^{-1}, if an ideal controller with $G_P = 1$ and $S_P = 0$ was used. Since an ideal controller is unrealizable in practice, the impedance realization performance of PBIC is determined by the bandwidth and accuracy of the position controller, while in FBIC the same applies with respect to the force controller [Koivisto et al., 2005].

3.1.3 Stability region of impedance parameters

Stability analysis of mechanical interaction between the manipulator and an environment is based on thermodynamic passivity. A realistic assumption is that the environment is passive – it can dissipate and store energy, but cannot create any on its own. The manipulator on the other hand can inject energy into the system, because compliance is created actively by feedback. For the interaction to be stable, the manipulator should therefore be made to behave passively, which means no more energy should be injected into the system than the system can naturally exhaust.

Impedance width, or Z-width, is a concept originating from the field of haptic teleoperation. Z-width is defined as the space of stable target impedance parameters, which means combinations of stiffness and damping that can be passively rendered by a certain mechanism [Boaventura et al., 2015]. Z-width can be graphically represented by using stiffness-damping plots, where the stability condition for a given frequency and sampling time is a line in the (k, b) -plane, which is illustrated in

Fig. 3.7. A more inclusive way to present Z-width would be a set of curves showing the upper and lower bounds of passively achievable impedances as a function of frequency.

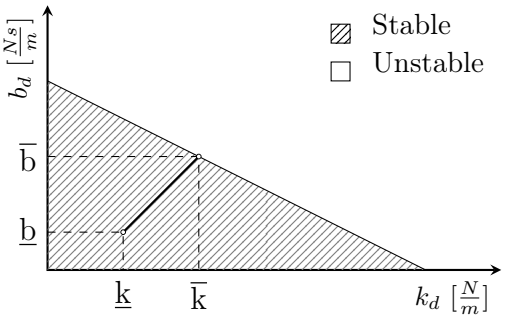

Figure 3.7 *Z-width illustrated, after [Koivumäki, 2016, p. 32].*

Effect of control gains on stability

Closed-loop bandwidth and steady-state error of the inner feedback loop has a major influence on both stability and performance of the outer feedback loop, which is why tuning of the inner loop is of critical importance for the impedance tracking capability and robustness of the impedance controller.

Lowering inner loop gains might improve stability, but at the cost of jeopardizing the inner loop performance and thus restricting the compliant behaviour of the manipulator. Respectively, increasing inner loop gains has a positive effect on impedance tracking performance, as it enlarges the closed-loop bandwidth and therefore range of frequencies for which the desired impedance can be emulated by the actuators. However, in cascade control both the inner and the outer control loop contribute to the total loop gain – in case the inner loop gain increases, the outer loop gain should reduce to maintain closed-loop stability. Gain scheduling could be applied to the control gains of the inner loop to adapt the bandwidth of the inner loop based on the chosen impedance parameters. [Focchi et al., 2016]

Consequently, trying to achieve higher bandwidth by increasing inner loop gains could reduce the region of stable impedance parameters. Therefore a compromise has to be made to find gains that provide a bandwidth high enough to ensure good impedance tracking and low enough to maintain a wide range of stable impedance parameters.

Effect of environment on stability

Environments can be divided into two extremes based on their low-frequency behaviour – springs act as impedances ($|Z_E(0)| = \infty$), while masses are equal to admittances ($|Z_E(0)| = 0$). Free space can be described as a mass-like inertial environment, while a rigid surface is a spring-like capacitive environment – the inverse of a capacitive system is inertial and vice versa. Capacitive environments ideally require force-controlled manipulators to make the manipulator inertial by feedback, while inertial environments require position-controlled manipulators to make the manipulator capacitive by feedback. [Lewis et al., 1993, p. 359–363]

Restriction to linear systems allows exploiting the various analytical tools provided by linear control theory. The literature concerning impedance control is rich in applying linear methods to analyze stability, and while these methods might not have much practical use in the controller design process, they nevertheless provide valuable insight on what sort of environments cause instability.

Coupled stability concerns interaction when the manipulator is mechanically coupled with an environment. If two objects are coupled, their interaction is equivalent to a unity-gain negative feedback connection of their impedance and admittance, illustrated in Fig. 3.8 below. Since coupling of two passive systems is guaranteed to be stable, the interaction is stable for any passive environment if the driving impedance of the manipulator is passive. [Buerger and Hogan, 2005, p. 10–11]

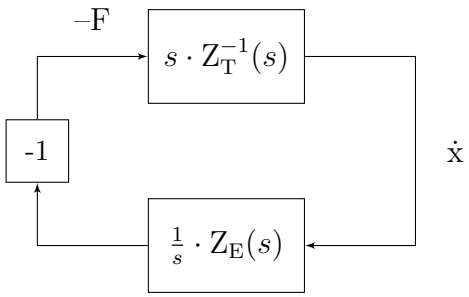

Figure 3.8 *Coupled manipulator-environment system.*

Coupled stability analysis is most often performed as serial connection of an ideally realized target impedance (assuming an ideal inner loop controller, i.e. a position-controller with $G_P = 1$ and $S_P = 0$) and a passive environment impedance, which is too conservative to be of use in practical contact tasks, considering the effects of unmodeled dynamics or communication and computation delays related to digital controller implementation [Vukobratovic et al., 2009, p. 48].

Analyzing stability boundaries of an impedance controller can be done by studying closed-loop impedance parameters. The ideal characteristic equation of the closed-loop system is

$$Z_T(s) + Z_E(s) = m_d \cdot s^2 + (b_d + b_e) \cdot s + (k_d + k_e) = 0 \ ,$$

[Salcudean et al., 2002] and for the system to be nominally stable, all the coupled system poles (i.e. solutions to the characteristic polynomial above) must lie in the left half-plane.

Another technique for analyzing coupled stability is the so called worst environment root locus test. Most challenging passive environments in terms of stability are lossless environments, which solely consist of energy-conserving elements (i.e. masses and springs) without energy-dissipating elements (i.e. dampers). Environments consisting of only masses or springs are therefore called most destabilizing environments. If the manipulator is stable when coupled to these troublesome 'worst environments', it is stable coupled to all passive environments. This remark allows analyzing coupled stability by means of two root locus plots – one parametrized by mass of a purely inertial environment and the other by the stiffness of a purely capacitive environment [Buerger and Hogan, 2005, p. 13]. This allows an alternative formulation of the coupled stability criterion to be derived – a sufficient condition for the plant to be stable when coupled to any arbitrary passive environment is that it is stable when coupled to all possible linear masses and all possible linear springs.

3.2 Controller implementation

Performance criteria for an impedance controller are shortly listed below, according to [Vukobratovic et al., 2009, p. 46]

- Accurate positioning in unconstrained free-space motion (i.e. when not in contact with the environment).
- A smooth contact transition to and from free-space motion (i.e. no oscillation or loss of contact after initial impact with the environment). Contact transition stability should be maintained interacting with the largest possible class of environments. Ideally contact transition stability is achieved when breaking and making contact with both high impedance environments (e.g. rocks) as well as with low impedance environments (e.g. sand).
- Exerting an appropriate force profile post-contact. The steady-state contact

force profile should correspond to the nominal force reference and impedance should increase to reflect how must the environment resists deformation.

In electrically actuated robots, due to linear current-torque -characteristics, so called disturbance observers can be used to estimate contact forces from current input and known robot dynamics. Impedance control without force sensing of any kind is not feasible in hydraulics, since the force produced by hydraulic cylinder is not solely dependent on valve control signal. A pressure-sensorless implementation would rely on knowing the environment characteristics precisely apriori and having an ideal position controller, both of which are practically infeasible assumptions.

The majority of literature concerning the application of impedance control for hydraulically actuated manipulators employs the position-based scheme. Therefore the position-based approach will also be followed in this thesis, since it has been found to be more suitable for hydraulic manipulators. A simple PBIC scheme for an excavator arm, in which the desired impedance of the end-effector is mapped onto the hydraulic cylinders using the arm Jacobian and a model of the arm gravity torques, is presented in Fig. 3.9.

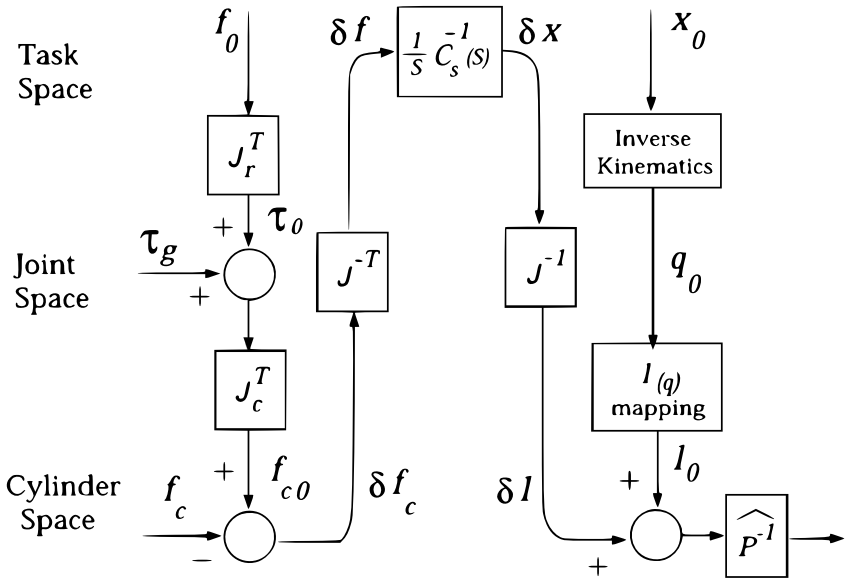

Figure 3.9 *Position-based impedance control, from [Salcudean et al., 2002].*

Gravity-compensated piston forces are mapped into end-effector forces by using the transposed inverse of arm Jacobian and the inverse Jacobian is used to map compliance to cylinder position commands. An explanation of the symbols in Fig. 3.9 is provided below:

f_0 is the vector of nominal force references

$\mathbf{J}_r^{\mathrm{T}}$ is the transpose of the joint Jacobian

τ_g is the vector of gravitational joint torques

$\mathbf{J}_c^{\mathrm{T}}$ is the transpose of the cylinder Jacobian

$\mathbf{J}^{-\mathrm{T}}$ is the inverse transpose of the Jacobian

$\frac{1}{s}C_s^{-1}$ is the target impedance filter

x_0 is the nominal position reference provided by the operator

$l(q)$ is the kinematic mapping from joint space to cylinder space

$\widehat{P^{-1}}$ is a stable inverse of the position control transfer function

3.2.1 Pressure-based contact force estimation

Force sensing for hydraulic cylinders can be realized either with load pins or indirectly by measuring chamber pressures. Load pins have a more sensitive and accurate response to external loads, but can be an order of magnitude more expensive and more problematic in terms of mechanical assembly [Salcudean et al., 2002]. Pressure sensors respond faster to changes in valve input, but have poor sensitivity for external forces and lower static accuracy mainly due to seal friction, which can practically never be fully compensated [Koivisto et al., 2005].

The piston force produced by a hydraulic cylinder equals to

$$f_c = p_1 \cdot A_1 - p_2 \cdot A_2 \ ,$$

where p_1, A_1, p_2 and A_2 symbolize the chamber pressures and effective areas on the piston and rod sides of the cylinder, respectively. The contact force can be roughly estimated by subtracting the effects of gravity, inertia and friction from the piston force as

$$\widehat{f}_{ext} = f_c - f_{gravity} - f_{inertia} - f_{friction}$$

If high force control precision is not a required and slow velocities and accelerations can be assumed, only a model of gravity torques might suffice, since motion torques can be assumed to be of negligible influence in contact situations. [Koivumäki, 2016, p. 10]

By combining the pressure signals from actuator space and the dynamic equations derived in configuration space and applying force transformations based on kinematics, we can separate the estimated contact force into directional components affecting in the workspace.

$$\widehat{\mathbf{F}}_{ext} = \mathbf{J}_x^{-\mathrm{T}}(\theta) \cdot \mathbf{J}_c^{\mathrm{T}}(\theta) \cdot \left[\; p_1 \cdot A_1 - p_2 \cdot A_2 \; \right] - \mathbf{J}_x^{-\mathrm{T}}(\theta) \cdot \left[\; \mathbf{I}(\theta) \cdot \ddot{\theta} + \mathbf{G}(\theta) \; \right] \tag{3.3}$$

The acquired force estimate should be low-pass filtered before being used for identification or control purposes.

3.2.2 Selection of impedance parameters

The design process for an impedance controller can be divided into two separate subtasks. The first task is to ensure proper realization and tracking of the target impedance, which concerns tuning of the inner loop controller. The second task is the stabilization of the target model, which means ensuring that chosen impedance parameters lead to stable establishment of contact, which is generally considered to be the most critical design issue in impedance controller synthesis. [Vukobratovic et al., 2009, p. 266]

When impedance is controlled separately in each direction of the operational space, the target impedance is chosen for each direction independently – high values for stiffness are selected in directions where positioning accuracy is important and the environment complies [Lawrence, 1988]. Accordingly, we shall choose the impedance along the Z-axis to be compliant, while the impedance along X-axis and Y-axis can be chosen relatively stiff. While coupling between impedances is possible, only uncoupled impedances will be considered in this thesis, which means matrices of impedance parameters $\mathbf{M}_d$, $\mathbf{B}_d$ and $\mathbf{K}_d$ are diagonal. Since only the impedance along Z-axis will be considered in this thesis, the impedance transfer function matrix assumes the simple form

$$\mathbf{Z}_T^{-1}(s) = \frac{1}{\mathbf{M}_d \cdot s^2 + \mathbf{B}_d \cdot s + \mathbf{K}_d} = \begin{bmatrix} 0 & 0 & 0 \\ 0 & 0 & 0 \\ 0 & 0 & \frac{1}{m_d \cdot s^2 + b_d \cdot s + k_d} \end{bmatrix}$$

Parametrization of the transfer functions in order to achieve certain contact dynamics is unintuitive as-is, but can be easened by expressing the target impedance by means of the generalized second-order system transfer function and solving it with respect to desired natural frequency ω_d and desired damping ratio ζ_d. Only taking into account the physical limitations of the manipulator and its control system is

not sufficient – at least a rough estimate of the environment dynamics is needed beforehand to achieve certain desired contact dynamics [Salcudean et al., 2002].

$$m_d \cdot s^2 + (b_d + b_e) \cdot s + (k_d + k_e) = \frac{\omega_d^2}{s^2 + 2 \cdot \zeta_d \cdot \omega_d \cdot s + \omega_d^2}$$

$$\Rightarrow \quad m_d = \sqrt{\frac{k_d + k_e}{\omega_d^2}} \ , \quad b_d + b_e = \zeta_d \cdot 2\sqrt{m_d \cdot (k_d + k_e)}$$

Certain considerations apply when tuning the impedance parameters in a way to ensure contact stability. Most importantly, the inner position feedback loop has a finite control bandwidth, so natural frequency has to be chosen accordingly – realizable natural frequencies for target impedance are practically only up to half of the position controller bandwidth. Secondly, physical capacity of the manipulator is a limiting factor to maximum attainable impedance.

An overdamped response is highly desirable for achieving contact stability, but the damping factor should not be chosen too large or otherwise sluggish behaviour shall cause force overshoot when establishing contact [Vukobratovic et al., 2009, p. 309]. For example, with a known valve control bandwidth of 2 Hz, and a desired end-effector stiffness of $10^6 \frac{N}{m}$ and an overdamped desired damping ratio of 1,5, we end up with the following continuous-time transfer function

$$Z_T^{-1}(s) = \frac{1}{6333 \cdot s^2 + 2,387 \cdot 10^5 \cdot s + 10^6} \ ,$$

with a settling time to within $\pm 1\%$ of the steady-state response of

$$t_{settling} = \frac{4,6}{\zeta_d \ \cdot \ \omega_d} \approx 0,85 \text{ s}$$

For digital controller implementation, the continuous-time impedance filter transfer function is discretized by means of bilinear transform (Tustin's approximation). The discretized transfer function is attained by replacing the Laplace-variable s by the relation $s = \frac{2}{T_s}\left(\frac{z-1}{z+1}\right)$, where T_s is the sampling time of the digital control system. The resulting discrete transfer function is an infinite impulse response (IIR) filter, which takes the following form

$$Z_T^{-1}(z) = \frac{1,134 \cdot 10^{-8} \cdot z^2 + 2,268 \cdot 10^{-8} \cdot z + 1,134 \cdot 10^{-8}}{z^2 - 1,413 \cdot z + 0,4587} \ ,$$

when using a sample period of 20 milliseconds.

The impedance control scheme described above was tested in simulation and it worked as intended. The impedance controller was successful in limiting external contact forces when the end-effector came into contact with a rigid contact surface.

4. EXPERIMENTS AND RESULTS

Due to a delay in the delivery and installation of pressure sensors on to the breaker plant, the initial objective of identifying dynamic parameters of the boom and testing the impedance controller couldn't be met. Therefore, the experimental part of this thesis consists of developing an automatic motion sequence for rock breaking applications tuning position control gains and times-of-flight (TOF) of motion trajectories, and finally determining the static and dynamic accuracy of the boom. A picture of the studied breaker boom is provided below in Fig. 4.1.

Figure 4.1 *The pedestal rock breaker boom studied in this thesis.*

Specific dimensions and components are confidential and cannot be openly published. The hardware setup consisted of a dSPACE MicroAutoBox II control system, which allows code generation from Mathworks' *Matlab/Simulink* models. dSPACE *ControlDesk* software was used for data visualization and to create a user interface from which the user can initiate the motion sequence by selecting locations from the grizzly. Joint angles were measured using absolute rotary encoders and a sample time of 10 ms was used throughout the experiments.

Since proportional valves are characterized by significant positive overlap of the spools, without deadzone compensation, large control action would be needed to get the valve over deadband area, which would require high gains and consequently result in a rough control signal [Münzer and Pedersen, 2002]. An overlap model, i.e. a lookup table describing the relation of spool position to volumetric flow, was identified[1] and is used as a compensation term, in order to lessen the effect valve nonlinearities and improve the dynamic response of the position controller.

4.1 Generation of the motion sequence

The sequence consists of movements between standby position to above the grid, an approach and a return movement along Z-axis, and a movement back to standby position. Quintic (i.e. fifth-order) polynomial trajectories [Jazar, 2010, p. 736] along Cartesian axes X, Y and Z were formed from the standby position to preprogrammed target points. The change of direction between the approach and return movements is a critical point, since in the worst case position overshoot could lead to the hammer hitting the grizzly. The highest point of the grizzly is located on ground level (at 0 meters expressed in the base coordinate frame Z-axis of the boom), which somewhat restricts the workspace of the planar arm along axes X and Y. A top-view of the grizzly screen and the locations of the standby position and the target points to be studied are illustrated in Fig. 4.2 below.

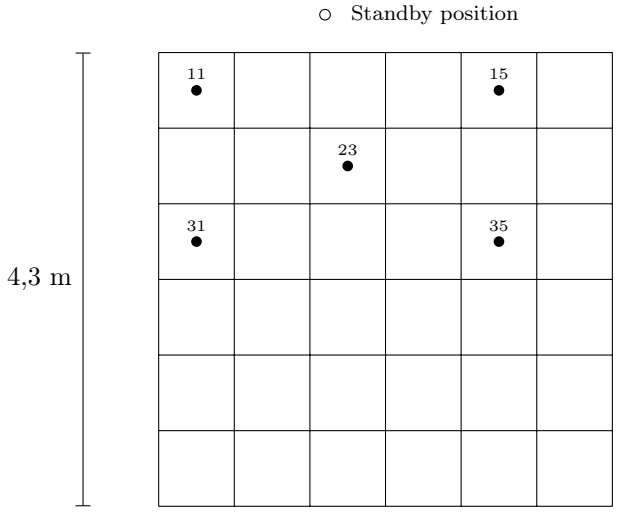

Figure 4.2 *Studied target points on the* 6×6 *grizzly screen.*

[1]For further information, see: *Automated feed-forward learning for pressure-compensated mobile hydraulic valves with significant dead-zone*, Nurmi J., Mattila J. (2017), ASME/BATH Symposium on Fluid Power and Motion Control

The performance was first tested with velocity feedforward only, the desired cylinder velocity being numerically differentiated from the cylinder position reference. Initially the TOF of the approach movement along Z-axis was chosen to be 8 seconds, while the TOF of the movement from standby position to above the target point 11 was fixed at 15 seconds. The result can seen in Fig. 4.3 below, where valve control signals are presented in the last plot.

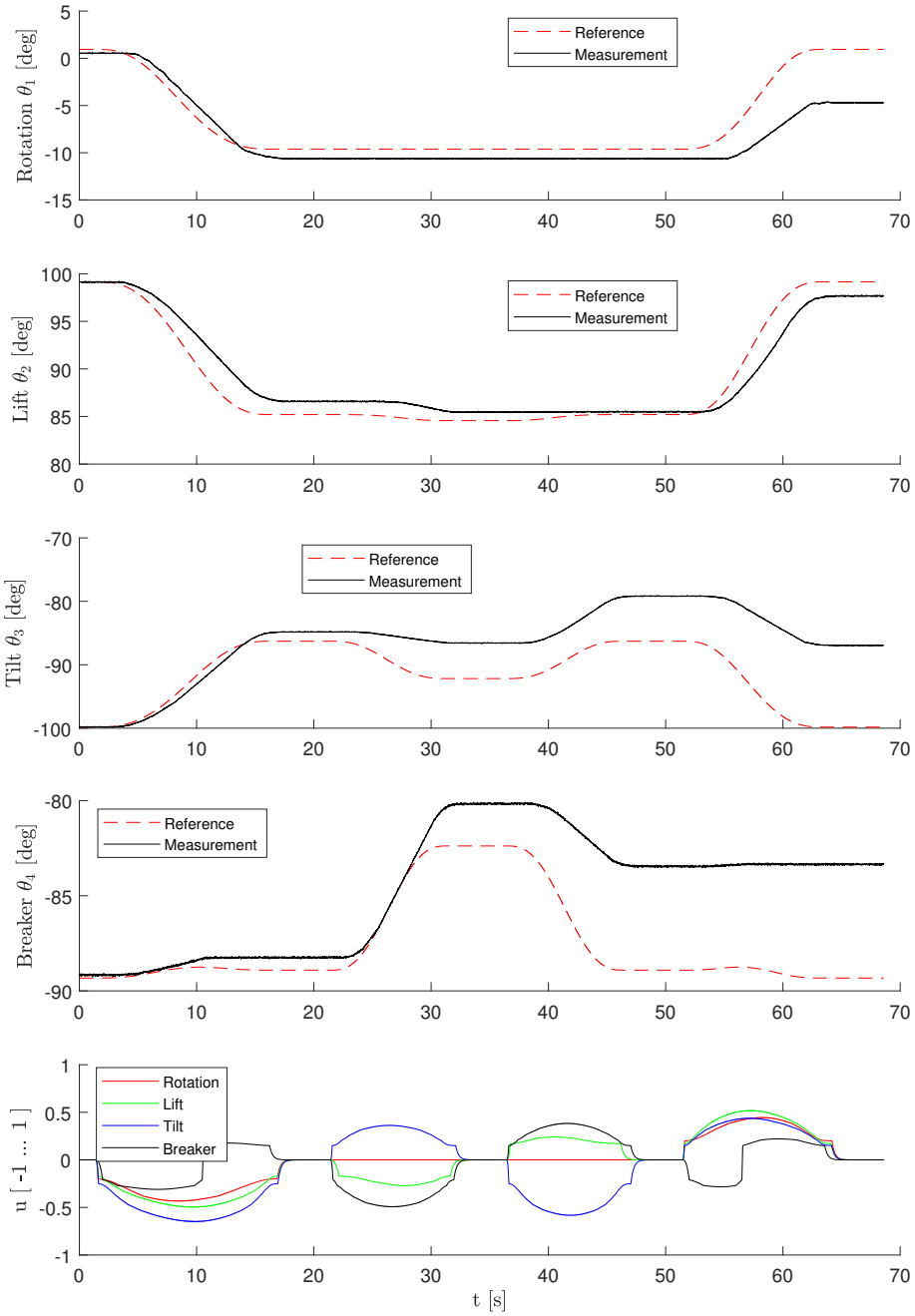

Figure 4.3 *Response with pure velocity feedforward.*

As the third plot of Fig. 4.3 shows, at around 25 second the tilt cylinder cannot follow the desired velocity propely, although its valve opening is not close to saturation. The models of spool flow acquired by idenfitication don't seem to match with reality what comes to positive control signals of the rotation motor and tilt cylinder.

When position feedback was applied, the results suggested that the initial TOF of 15 seconds seems to be too short the farthest target point, causing significant dynamic error of up to 0,5 meters in addition to visible jerk during movement. The TOFs should be dynamically determined based on the distance to the specific target point, but this is left for future optimization and for now suitable values were chosen as a compromise, in order to ensure desired velocities that are achievable even when reaching for the farthest target point. In the following sections, a position feedback controller is tuned and tested, first separately and finally in combination with velocity feedforward for comparison.

4.2 Tuning of the position controller

After introducing deadzone compensation, which allows loosening the gains to get the same performance, there still exists ways to increase control gains without facing instability. Compared to conventional P-control, filtered P-control allows increasing proportional gains K twice or thrice at low frequencies since the high-frequency gain is filtered out. Time constants τ of the first-order low-pass filter can be selected with a rule of thumb which suggests that τ should be two to three times the mimimum hydraulic natural frequency $\omega_{h,min}$. [Linjama, 1996, p. 80–81]

$$\tau = \frac{2 \ldots 3}{\omega_{h,min}}$$

The resulting position control transfer function matrix is

$$\mathbf{C}_P(s) = \begin{bmatrix} \frac{K_1}{\tau_1 \cdot s+1} & 0 & 0 & 0 \\ 0 & \frac{K_2}{\tau_2 \cdot s+1} & 0 & 0 \\ 0 & 0 & \frac{K_3}{\tau_3 \cdot s+1} & 0 \\ 0 & 0 & 0 & \frac{K_4}{\tau_4 \cdot s+1} \end{bmatrix}$$

The natural frequency of a hydraulic cylinder is a function of piston position – for an asymmetric cylinder, the maximum natural frequency is achieved in the negative end of the cylinder, when the piston is fully retracted. The minimum natural frequency is achieved slightly on the positive side from the middle position of the piston, from where it increases slowly when extending the cylinder. [Lammela, 1990, p. 6]

The minimum natural frequency was experimentally identified by moving the actuators at fast pace and applying a sudden change of direction in order to get them to oscillate. The largest period of oscillation was found to be around 0,7 seconds, which corresponds to a minimum frequency of 8,9760 rad/s and a filter time constant between 0,2228 to 0,3342 seconds. The tuned controller parameters are presented in Table 4.1.

Table 4.1 *Tuned filter time constants and proportional gains for each joint.*

n	θ_1	θ_2	θ_3	θ_4
τ_n	0,2228	0,2228	0,2228	0,2228
K_n	0,5	0,7	0,7	0,6

Used performance measures for path tracking are the maximum value of Cartesian position error ΔC of the tool tip (i.e. dynamic accuracy), which is calculated as

$$\Delta C = \sqrt{(x_0 - x)^2 + (y_0 - y)^2 + (z_0 - z)^2} \ ,$$

and Cartesian steady-state position error (i.e. static accuracy). The TOF of the approach movement along Z-axis was fixed at 10 seconds, while the TOF of the movement from standby position to above the target point 11 was fixed at 15 seconds and the TOF of the movement from standby position to above the target point 35 was fixed at 20 seconds. The response with filtered P-control for target point 11 is presented in Fig. 4.4 and 4.5, and for target point 35 in Fig. 4.6 and 4.7. Similar plotted responses for the rest of the studied target points using filtered P-control tuned with the parameters presented in Table 4.1 can be found in Appendix B.

The results suggest that the rotation motor is a significant source of tracking error in closed-loop control. We can see from Fig. 4.7 that the Y-axis has a steady-state error of about 3 cm is solely due to the rotation motor. Meanwhile, in the last plot of Fig. 4.6 the control signal of the rotation valve is oscillating around zero, which would suggest that too high control gains are being used. It can be noted from the first plots of Fig. 4.4 and Fig. 4.6 that the response of the rotation motor has significant lag on positive openings, which causes dynamic error during motion. Meanwhile the negative openings seem to track position well during motion, but ends up with notable steady-state error at rest. Since the response for positive and negative openings is asymmetric, most of the poor performance can likely be attributed to poorly identified and thus uncompensated deadband of the positive opening of the rotation valve.

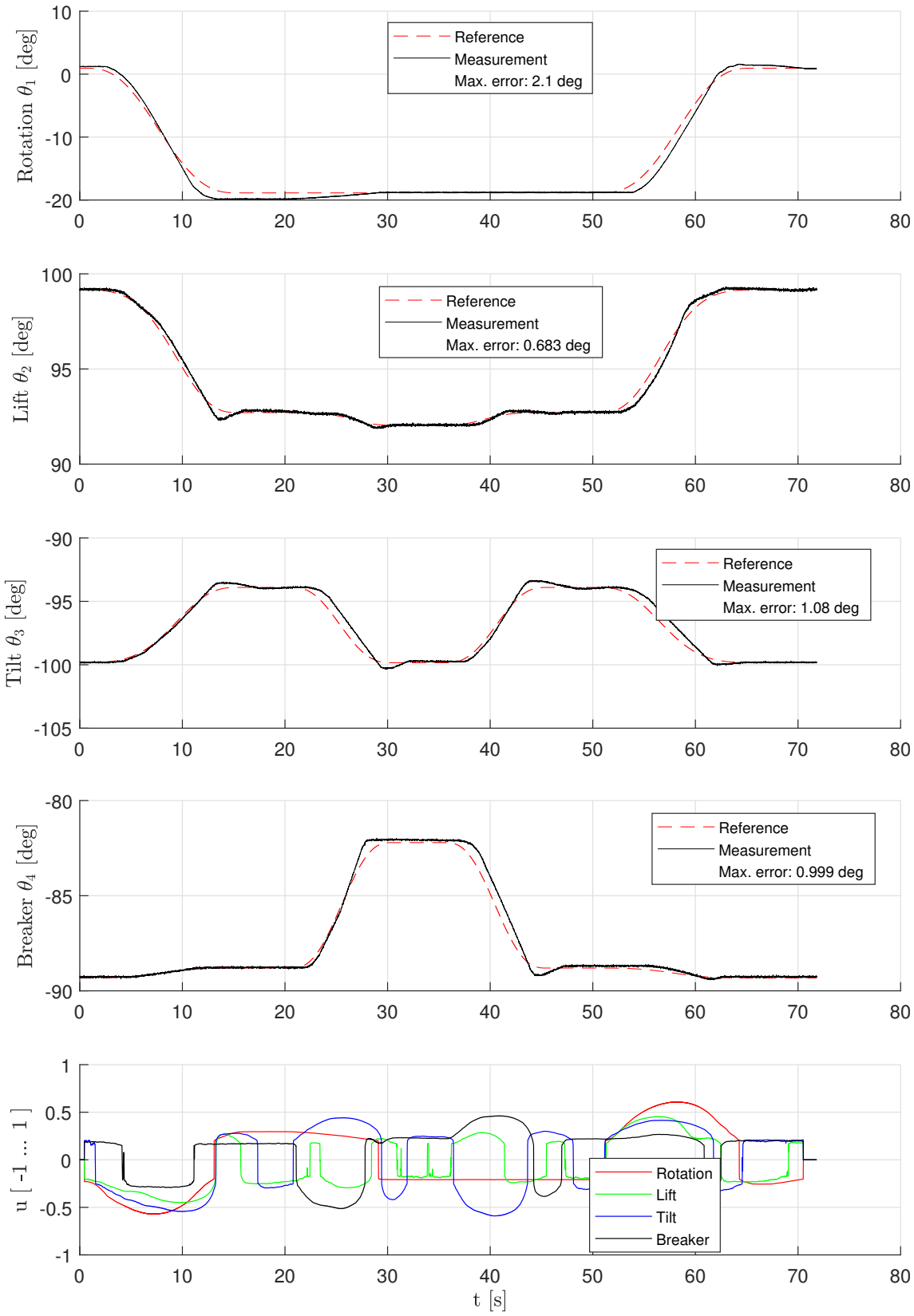

Figure 4.4 *Tracking performance for target point 11 with filtered P-control.*

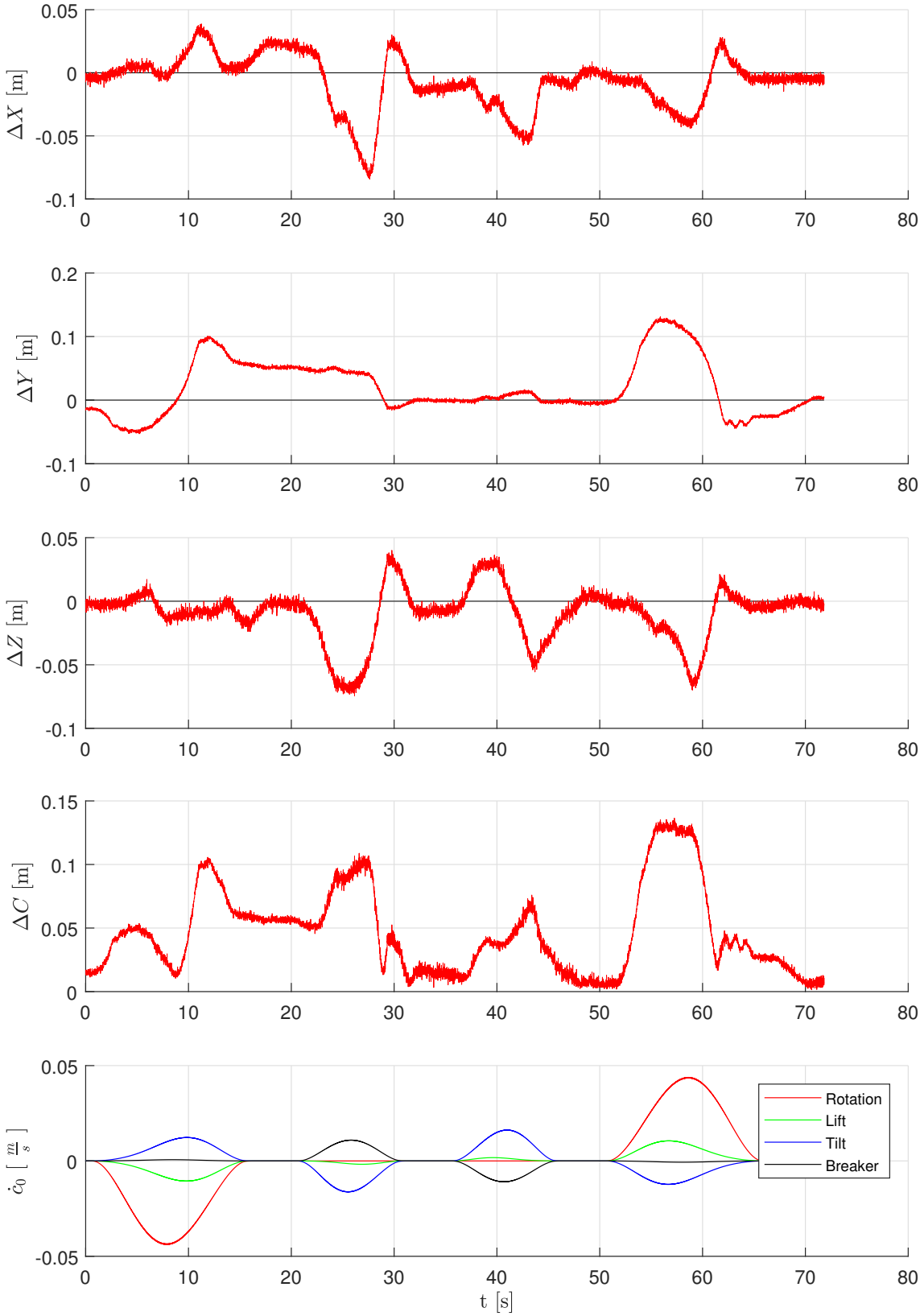

Figure 4.5 *Cartesian error for target point 11 with filtered P-control.*

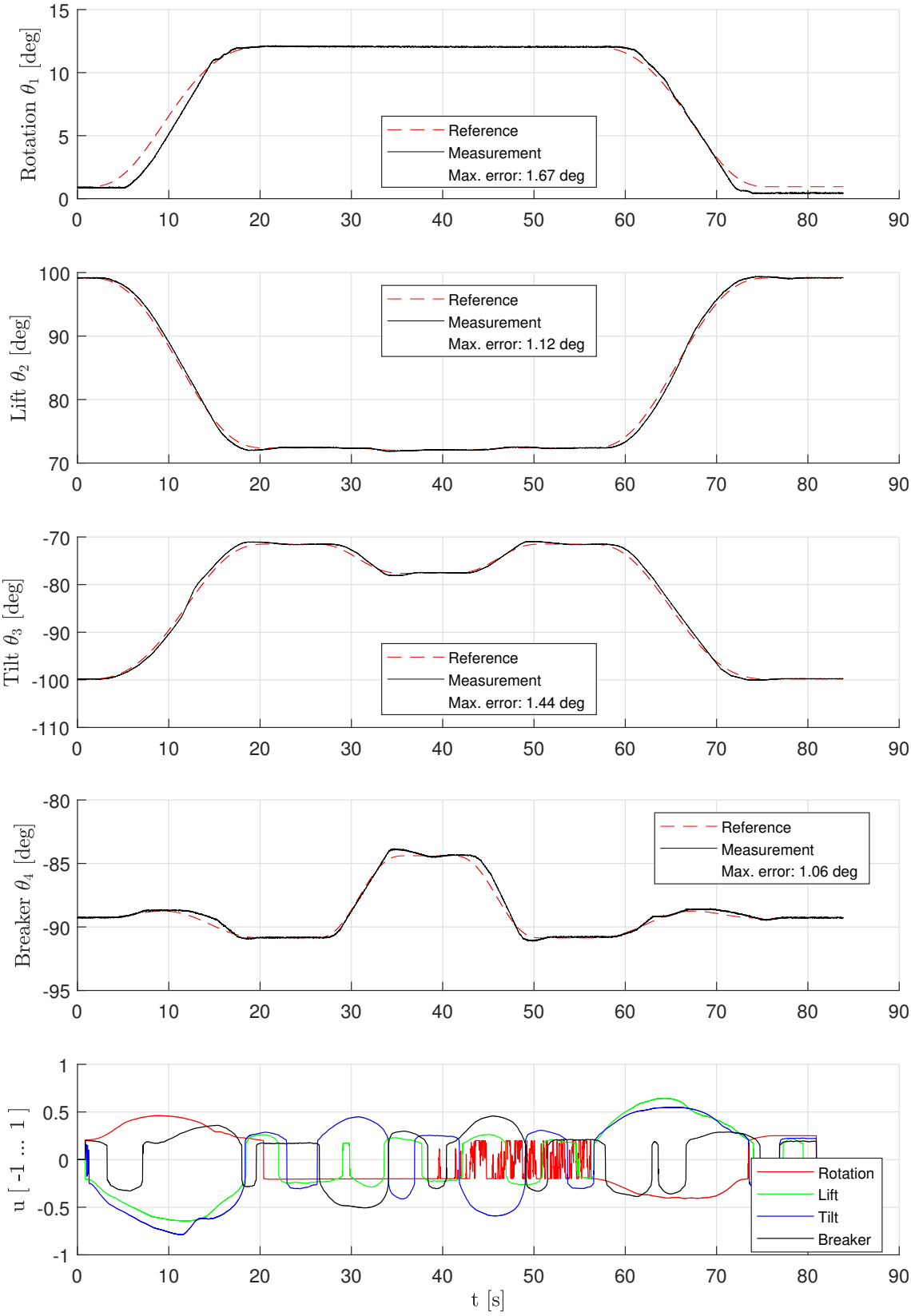

Figure 4.6 *Tracking performance for target point 35 with filtered P-control.*

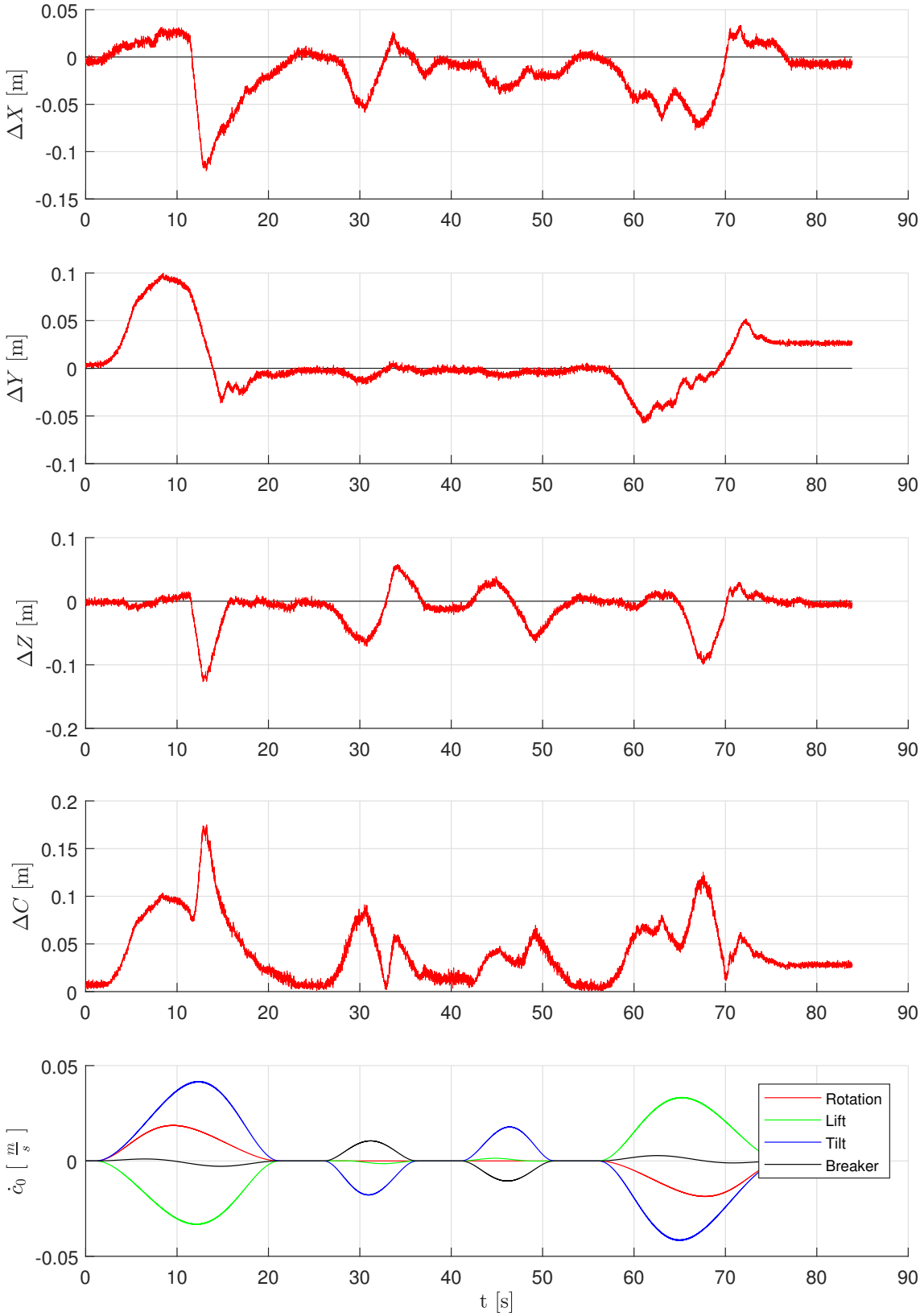

Figure 4.7 *Cartesian error for target point 35 with filtered P-control.*

Next, the response for equivalent trajectories with filtered P-control combined with velocity feedforward was evaluated. The results for target point 11 are presented in Fig. 4.8 and 4.9, and for target point 35 in Fig. 4.10 and 4.11. It can be concluded introducing velocity feedforward had a slightly negative effect on the dynamic accuracy of the boom in this particular case. However, velocity feedforward did smoothen the control signal of the rotation valve, while the static accuracy remained practically the same.

Tuning parameters in a way to ensure performance and stability in the whole workspace of the manipulator was shown to be a challenging task. The maximum Cartesian error of the hammer tip was up to 17 cm, which leaves some room for improvement. In this application, the dynamic accuracy is not of greatest importance when moving from standby position to above the target points and could be compromised, as long as the steady-state error remains low. The Cartesian static error as well as the Cartesian dynamic error was mainly due to the poor performance of the rotation motor, which resulted in disproportionately large tracking errors on the Cartesian Y-axis.

During the approach movement, position overshoots of up to 10 centimeters occured on the Z-axis. This means the boom can safely be commanded position references up to this distance above the highest point of the grid, provided with some additional margin of safety. This suggests the boom can be driven back to standby position in the proximity of the grizzly, which could allow to shorten the TOF of the return movement and bring down total execution time of the sequence.

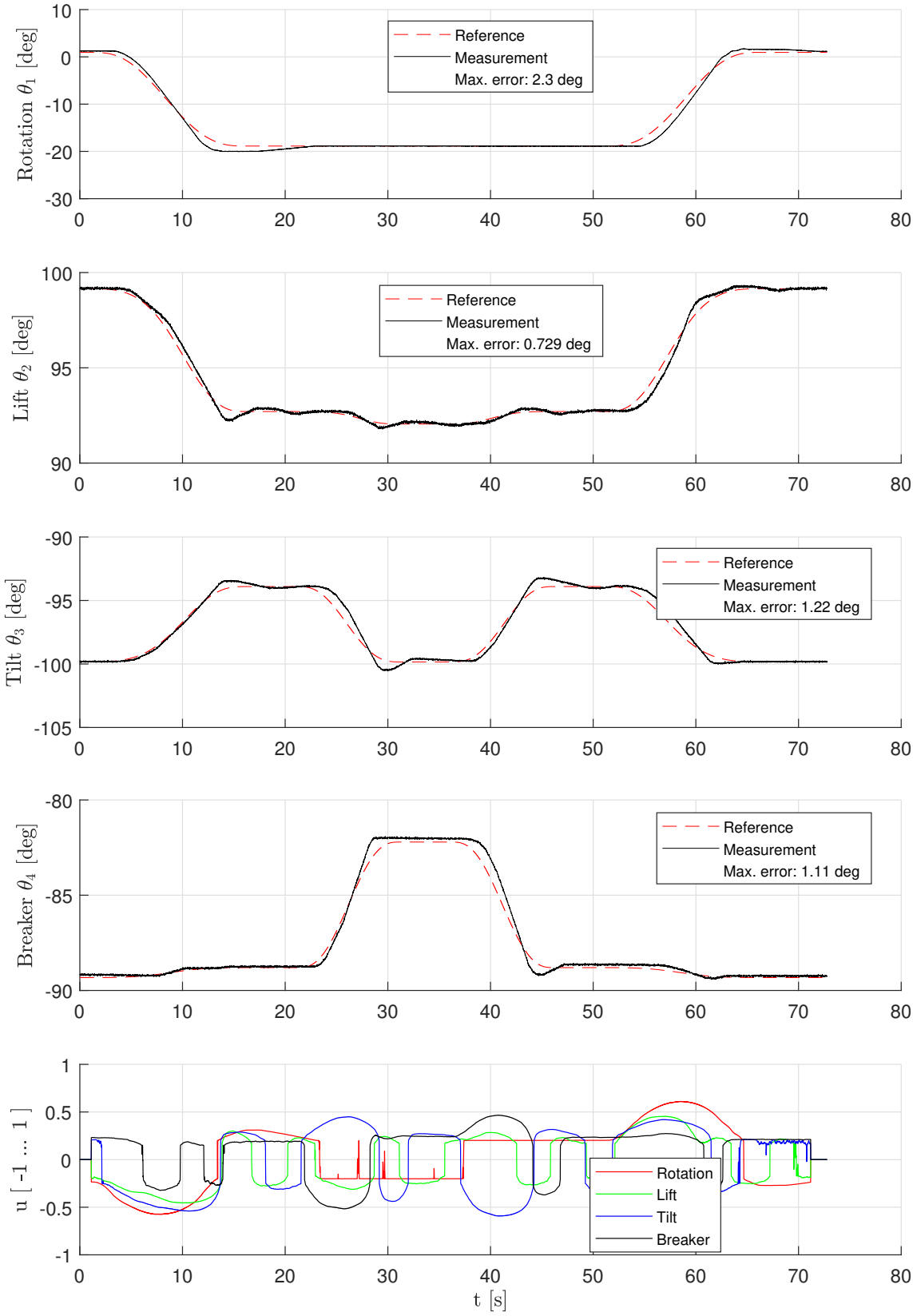

Figure 4.8 *Tracking error for target point 11 after adding velocity feedforward.*

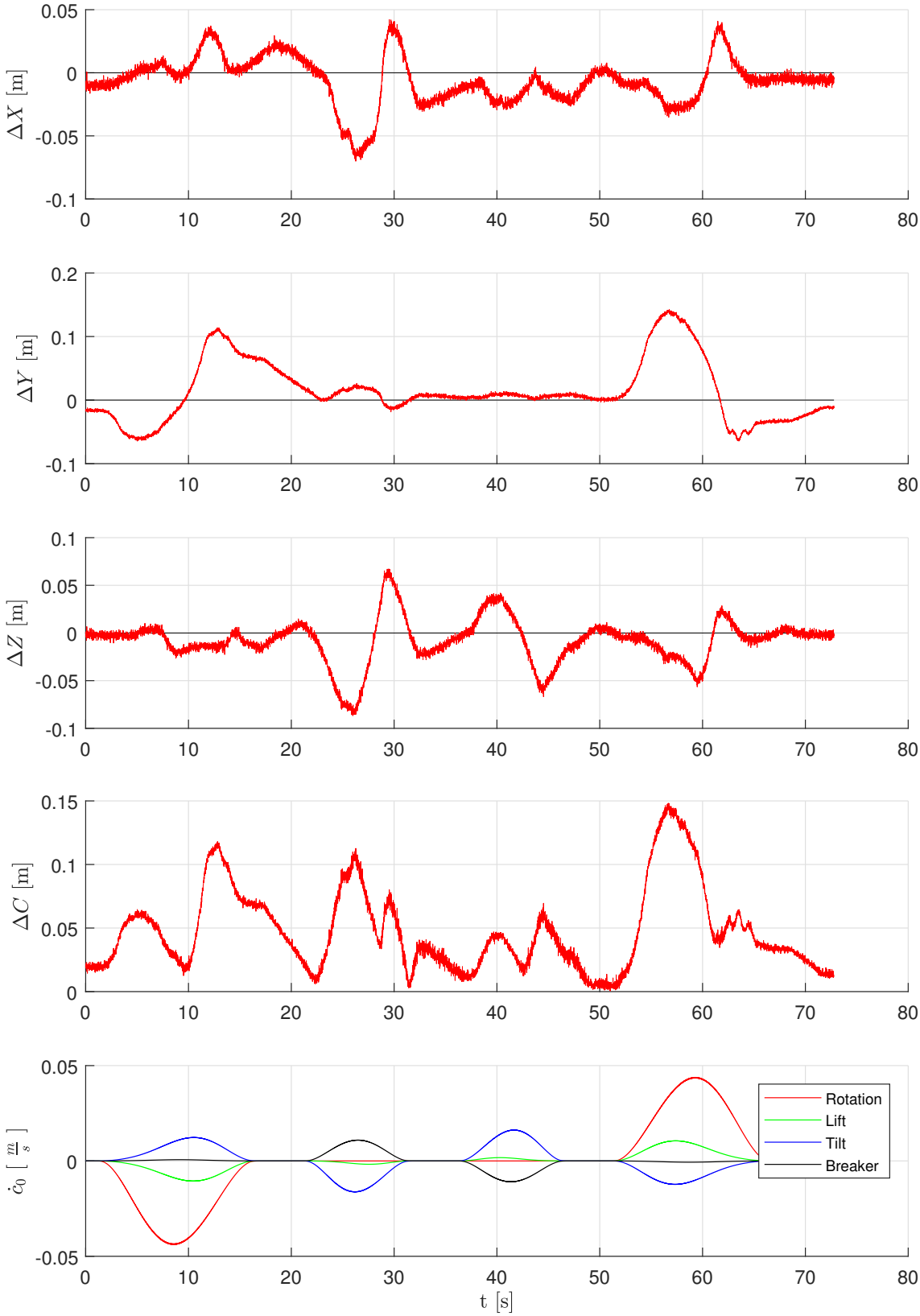

Figure 4.9 *Cartesian error for target point 11 after adding velocity feedforward.*

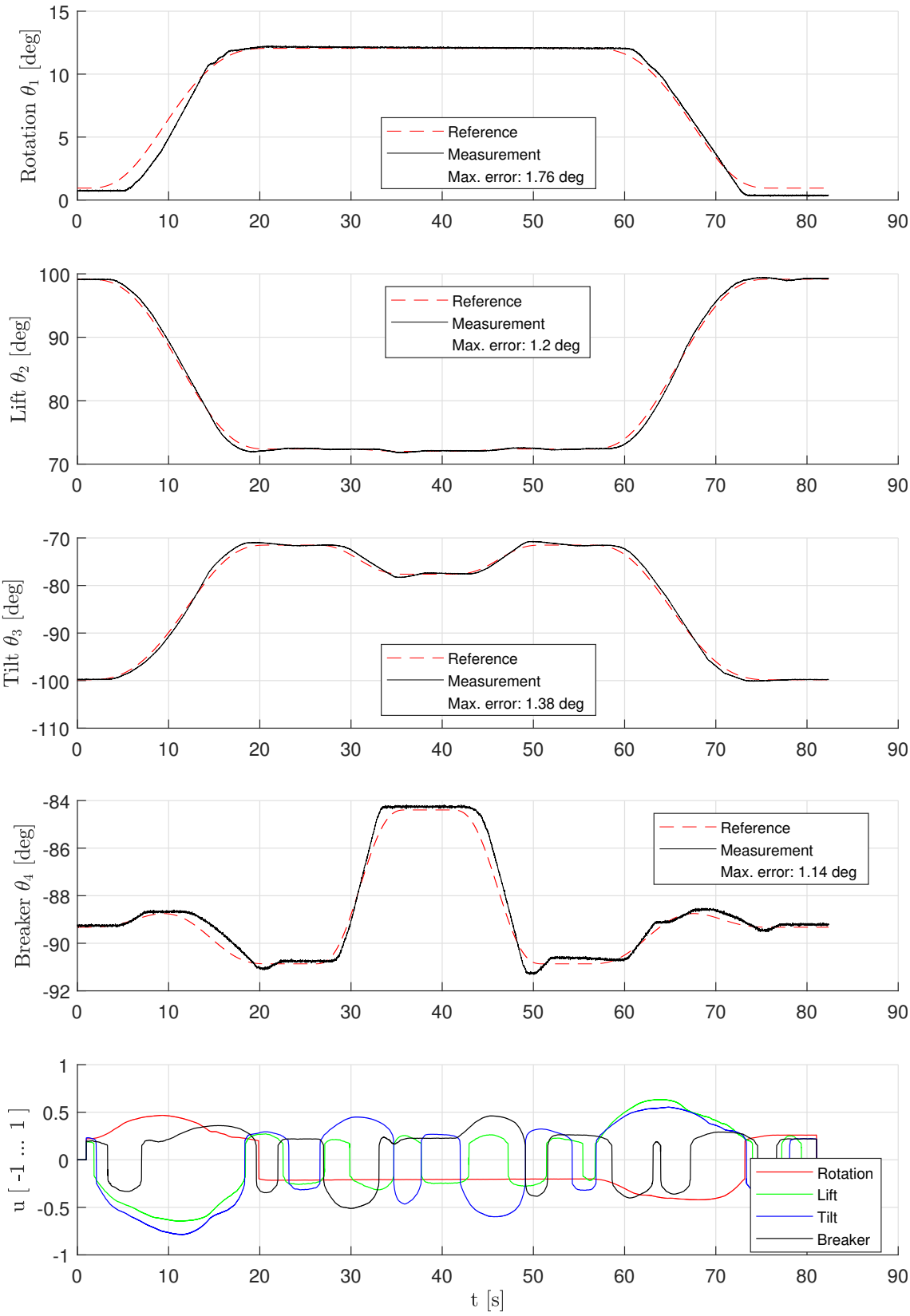

Figure 4.10 *Tracking error for for target point 35 after adding velocity feedforward.*

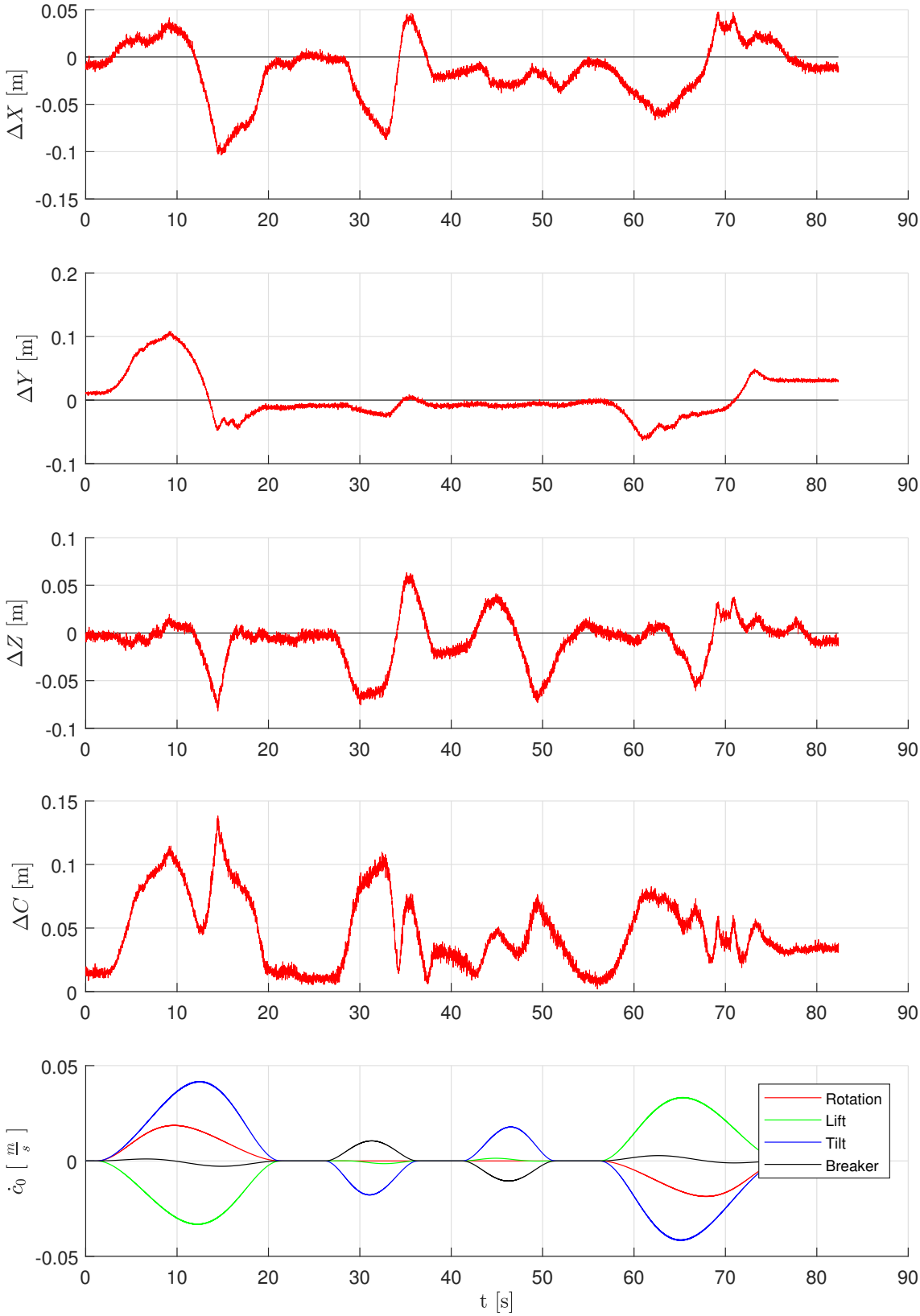

Figure 4.11 *Cartesian error for target point 35 after adding velocity feedforward.*

5. SUMMARY AND CONCLUSIONS

In this thesis, an impedance controller for a hydraulic manipulator was developed and tested in simulation, and an automatic motion sequence for a rock breaker boom was developed. The theoretical part of this thesis covered kinematics and dynamics of the breaker boom and provided an overview of position-based impedance control and its limitations. The experimental part of the thesis consisted of tuning a joint position controller to examine the dynamic and static accuracy of the position-controlled boom.

The carried experiments suggest that the boom can only operate at relatively low velocities in closed-loop control, and therefore active compliance on the tool tip might not provide significant added value, although the contact force estimation scheme could be useful for detecting contact even without regulation of impedance. However, in comparison to the studied large-scale stationary boom, it would be interesting to see whether the feasibility of impedance-like contact control would be different for smaller-scale breaker booms in mobile crushing plants. Small breaker booms in mobile crushers might have relatively faster movements and their workspace is likely more limited due to obstacles, which makes the risk of collision with expensive hardware more imminent.

Achieving good position tracking performance was found to be a challenging task. The low closed-loop control performance of the rotation motor, which was at least partially due to an unperfect model of valve deadzone, seemed to limit the tracking capability in Cartesian space. The resulting accuracy after controller tuning was a maximum Cartesian error of about 17 centimeters during movement, while the maximum Cartesian steady-state error was about 3 centimeters. By addressing the low performance of the rotation motor with an improved deadzone inverse model of the rotation valve, dynamic accuracy could likely be improved inside the range of 10 centimeters without introducing additional controller parameters. While the filtered P-controller has the advantage of having a small number of parameters, tuning the plant manually during commissioning is time-consuming, which could be an argument for a more sophisticated controller with adaptive capabilities.

Besides fixing the performance issues related to the rotation motor, suggestions for future improvements for the rock breaking sequence include an impaction detection scheme based on inertial measurement units. Since the boom is equipped with inertial measurements units for joint angle estimation, exploiting linear acceleration data or angular velocity data to detect disturbances during the approach movement could be a preferable alternative to pressure-based contact force estimation.

REFERENCES

[Boaventura et al., 2015] Boaventura, T., Buchli, J., Semini, C., and Caldwell, D. G. (2015). Model-Based Hydraulic Impedance Control for Dynamic Robots. *IEEE Transactions on Robotics*, 31(6):1324–1336.

[Buerger and Hogan, 2005] Buerger, S. P. and Hogan, N. (2005). Impedance and interaction control. In Kurfess, T., editor, *Robotics and Automation Handbook*, chapter 19, pages 368–391. Taylor & Francis.

[Colgate, 1989] Colgate, J. E. (1989). On the intrinsic limitations of force feedback compliance controllers. *Proceedings of ASME Winter Annual Meeting 1989*, 14:23–30.

[Craig, 2005] Craig, J. (2005). *Introduction to Robotics: Mechanics and Control*. Pearson Prentice Hall, 3rd edition.

[De Schutter et al., 1997] De Schutter, J., Bruyninckx, H., Zhu, W.-H., and Spong, M. W. (1997). Force control: A bird's eye view. *IEEE CSS/RAS International Workshop on Control Problems in Robotics and Automation: Future Directions*, pages 1–17.

[Focchi et al., 2016] Focchi, M., Medrano-Cerda, G. A., Boaventura, T., Frigerio, M., Semini, C., Buchli, J., and Caldwell, D. G. (2016). Robot impedance control and passivity analysis with inner torque and velocity feedback loops. *Control Theory and Technology*, 14(2):97–112.

[Jazar, 2010] Jazar, R. N. (2010). *Theory of Applied Robotics: Kinematics, Dynamics, and Control*. Springer Publishing Company, 2nd edition.

[Koivisto et al., 2005] Koivisto, H., Mattila, J., Mäkelä, A., Siuko, M., and Vilenius, M. (2005). On pressure/force control of a water hydraulic joint. *Proceedings of the Ninth Scandinavian International Conference on Fluid Power, SICFP'05, June 1.-3, 2005, Linköping, Sweden*, pages 1–14.

[Koivumäki, 2016] Koivumäki, J. (2016). *Stability-Guaranteed Nonlinear Model-Based Control of Hydraulic Robotic Manipulators*. PhD thesis, Tampere University of Technology.

[Lammela, 1990] Lammela, J. (1990). *Digitaalinen tilasäätäjä ja tarkkalilija hydrauliservossa*. Master's thesis, Tampere University of Technology.

[Lawrence, 1988] Lawrence, D. A. (1988). Impedance control stability properties in common implementations. *Proceedings of the 1988 IEEE International Conference on Robotics and Automation*, 2:1185–1190.

[Lewis et al., 1993] Lewis, F. L., Dawson, D. M., and Abdallah, C. T. (1993). *Control of Robot Manipulators*. Macmillan Publishing Company, New York.

[Linjama, 1996] Linjama, M. (1996). *Modelling of Flexible Hydraulic Manipulators*. PhD thesis, Tampere University of Technology.

[Lovgren, 2004] Lovgren, R. (2004). Radical improvements in crane safety. *ISO focus*, 1(7):21–93.

[Metso Mining and Construction, 2015] Metso Mining and Construction (2015). *Basics in Minerals Processing Handbook*.

[Münzer and Pedersen, 2002] Münzer, M. E. and Pedersen, P. (2002). Tool centre control of mobile hydraulic manipulators. *2nd International FPNI PhD Symposium on Fluid Power, Modena, Italy, 2002.*

[Muhammad et al., 2009] Muhammad, A., Mattila, J., Virvalo, T., and Vilenius, M. (2009). Force-based and position-based impedance control of hydraulic manipulators. *The 11th Scandinavian International Conference on Fluid Power SICFP'09, Linköping, Sweden, June 2-4 2009*, pages 327–341.

[Ott et al., 2015] Ott, C., Mukherjee, R., and Nakamura, Y. (2015). A hybrid system framework for unified impedance and admittance control. *Journal of Intelligent & Robotic Systems*, 78(3):359–375.

[Salcudean et al., 2002] Salcudean, S. E., Tafazoli, S., Hashtrudi-Zaad, K., and Lawrence, P. D. (2002). Impedance control of a teleoperated excavator. *IEEE Transactions on Control Systems Technology*, 10(3):355–367.

[Sandvik Mining and Construction, 2016] Sandvik Mining and Construction (2016). *Hydraulic Hammer Rammer 2577, Operator's Manual*. Available at `https://www.rammer.com/en/products/hydraulic-hammers/excellence-line/medium-range/2577/`.

[Sciavicco et al., 2000] Sciavicco, L., Siciliano, B., and Sciavicco, B. (2000). *Modelling and Control of Robot Manipulators*. Springer-Verlag, London, 2nd edition.

[Tafazoli, 1997] Tafazoli, S. (1997). *Identification of frictional effects and structural dynamics for improved control of hydraulic manipulators*. PhD thesis, University of British Columbia.

[Valency and Zacksenhouse, 2003] Valency, T. and Zacksenhouse, M. (2003). Accuracy/robustness dilemma in impedance control. *ASME Journal of Dynamic Systems Measurement and Control*, 125(3):310–319.

[Vukobratovic et al., 2009] Vukobratovic, M., Surdilovic, D., Ekalo, Y., and Katic, D. (2009). *Dynamics and Robust Control of Robot-environment Interaction*. New Frontiers in Robotics – Vol. 2. World Scientific Publishing, Singapore.

APPENDIX A: MATLAB-CODE FOR INVERSE ARM DYNAMICS

```
function tau = invdyn(theta,thetadot,thetadotdot)

% define the following parameters
% r2 r3 r4 L2 L3 m2 m3 m4 I2 I3 I4

theta2dotdot=thetadotdot(2);
theta3dotdot=thetadotdot(3);
theta4dotdot=thetadotdot(4);

theta2dot=thetadot(2);
theta3dot=thetadot(3);
theta4dot=thetadot(4);

theta2=theta(2); theta3=theta(3); theta4=theta(4);

 %% INERTIAL TERMS

tau4i = (I4+m4*r4^2)*theta2dotdot + (I4+m4*r4^2)*
   theta3dotdot + (I4+m4*r4^2)*theta4dotdot + m4*r4*L2*
   theta2dotdot*cos(theta3 + theta4) + m4*r4*L3*
   theta2dotdot*cos(theta4) + m4*r4*L3*theta3dotdot*cos(
   theta4)
tau3i = tau4i + (I3+m3*r3^2)*theta2dotdot + (I3+m3*r3^2)*
   theta3dotdot + m4*r4*L3*theta2dotdot*cos(theta4) + m4*
   r4*L3*theta3dotdot*cos(theta4) + L3^2*m4*theta2dotdot
   + L3^2*m4*theta3dotdot + L2*L3*m4*theta2dotdot*cos(
   theta3) + L2*m3*r3*theta2dotdot*cos(theta3) + m4*r4*L3
   *theta4dotdot*cos(theta4)
tau2i = tau3i + (I2+m2*r2^2)*theta2dotdot + L2^2*m3*
   theta2dotdot + L2^2*m4*theta2dotdot + L2*L3*m4*
   theta2dotdot*cos(theta3) + L2*m3*r3*theta2dotdot*cos(
   theta3) + 2*L2*m4*r4*theta2dotdot*cos(theta3 + theta4)
    + m4*r4*L2*theta4dotdot*cos(theta3 + theta4) + L2*L3*
   m4*theta3dotdot*cos(theta3) + L2*m3*r3*theta3dotdot*
   cos(theta3)
```

```
 %% CENTRIGUGAL AND CORIOLIS TERMS

tau4c = - m4*r4*L2*theta2dot*sin(theta3+theta4)*(
   theta3dot+theta4dot) - m4*r4*L3*theta2dot*theta4dot*
   sin(theta4) - m4*r4*L3*theta3dot*theta4dot*sin(theta4)
tau3c = - L3*m4*r4*theta4dot^2*sin(theta4) - L2*m4*r4*
   theta2dot*sin(theta3+theta4)*(theta3dot + theta4dot) -
    L2*L3*m4*theta2dot*theta3dot*sin(theta3) - L2*m3*r3*
   theta2dot*theta3dot*sin(theta3) - 2*L3*m4*r4*theta2dot
   *theta4dot*sin(theta4) - 2*L3*m4*r4*theta3dot*
   theta4dot*sin(theta4)
tau2c = - L2*L3*m4*theta3dot^2*sin(theta3) - L2*m3*r3*
   theta3dot^2*sin(theta3) - L3*m4*r4*theta4dot^2*sin(
   theta4) - 2*L2*m4*r4*theta2dot*sin(theta3+theta4)*(
   theta3dot+theta4dot) - L2*m4*r4*theta3dot*sin(theta3+
   theta4)*(theta3dot+theta4dot) - L2*m4*r4*theta4dot*sin
   (theta3+theta4)*(theta3dot+theta4dot) - 2*L2*L3*m4*
   theta2dot*theta3dot*sin(theta3) - 2*L2*m3*r3*theta2dot
   *theta3dot*sin(theta3) - 2*L3*m4*r4*theta2dot*
   theta4dot*sin(theta4) - 2*L3*m4*r4*theta3dot*theta4dot
   *sin(theta4)

 %% GRAVITATIONAL TERMS

 g = -9.81;              % gravitational acceleration

tau4g = m4*g*r4*cos(theta2+theta3+theta4);
tau3g = tau4g + (m4)*g*L3*cos(theta2+theta3) + m3*g*r3*
   cos(theta2+theta3);
tau2g = tau3g + (m3+m4)*g*L2*cos(theta2) + m2*g*r2*cos(
   theta2);

tau = [ tau2i+tau2c+tau2g
        tau3i+tau3c+tau3g
        tau4i+tau4c+tau4g; ];

end
```

APPENDIX B: TRACKING PERFORMANCE FOR TARGET POINTS

In the following pages, tracking performance with filtered P-control is presented for the target points 31 (Fig. B.1 and B.2), 15 (Fig. B.3 and B.4) and 23 (Fig. B.5 and B.6).

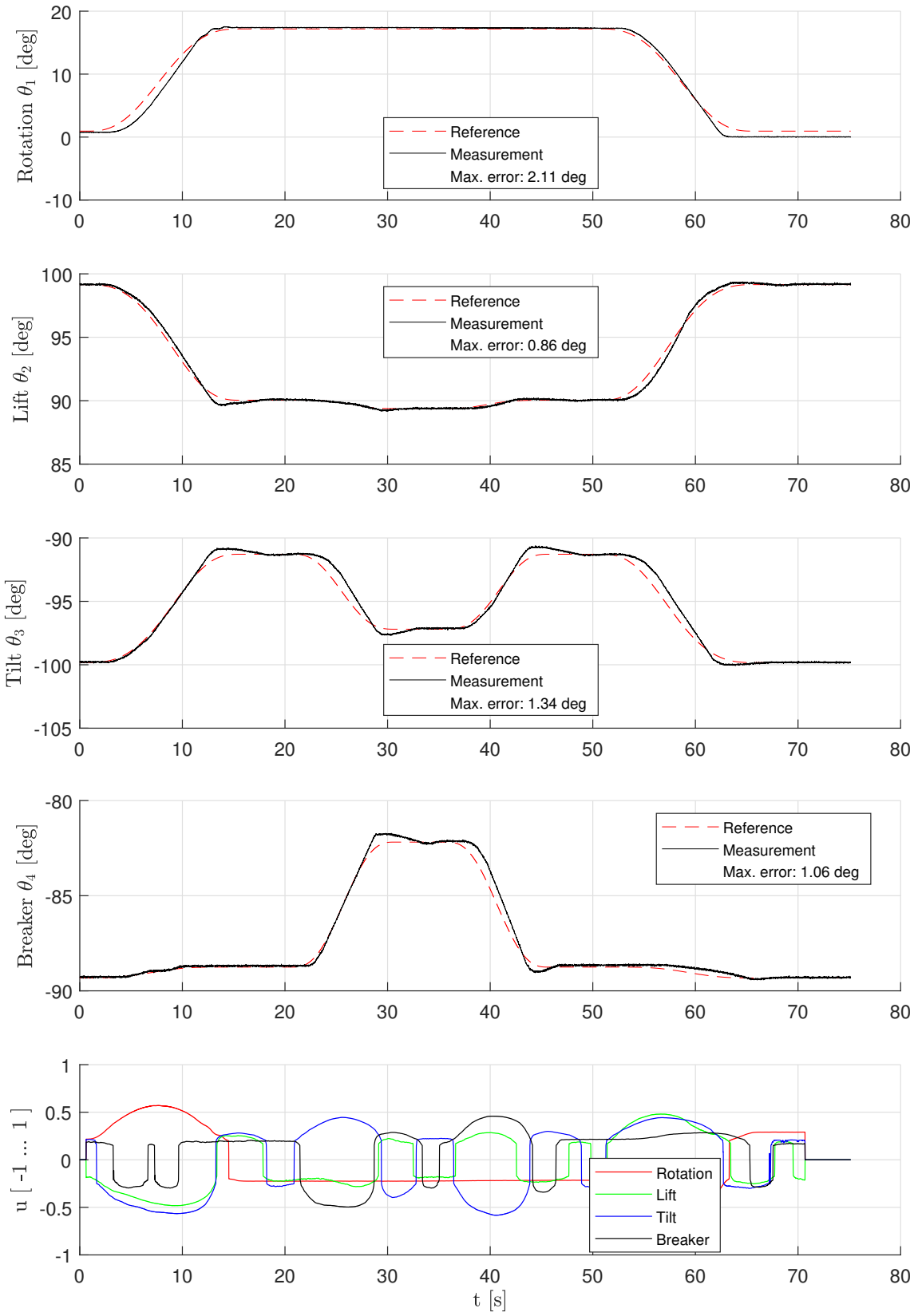

Figure B.1 *Tracking error for target point 15 with filtered P-control.*

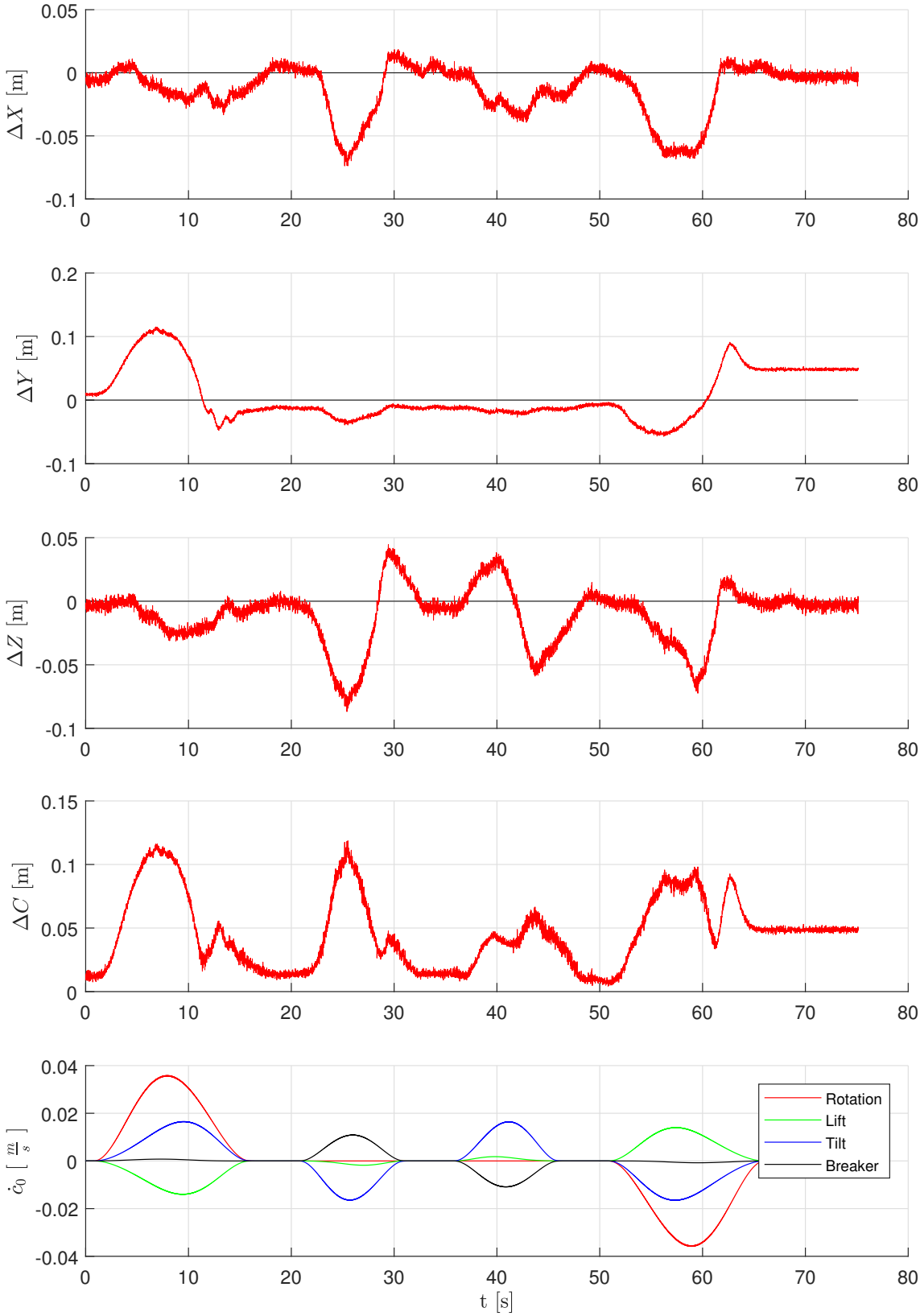

Figure B.2 *Cartesian error for target point 31 with filtered P-control.*

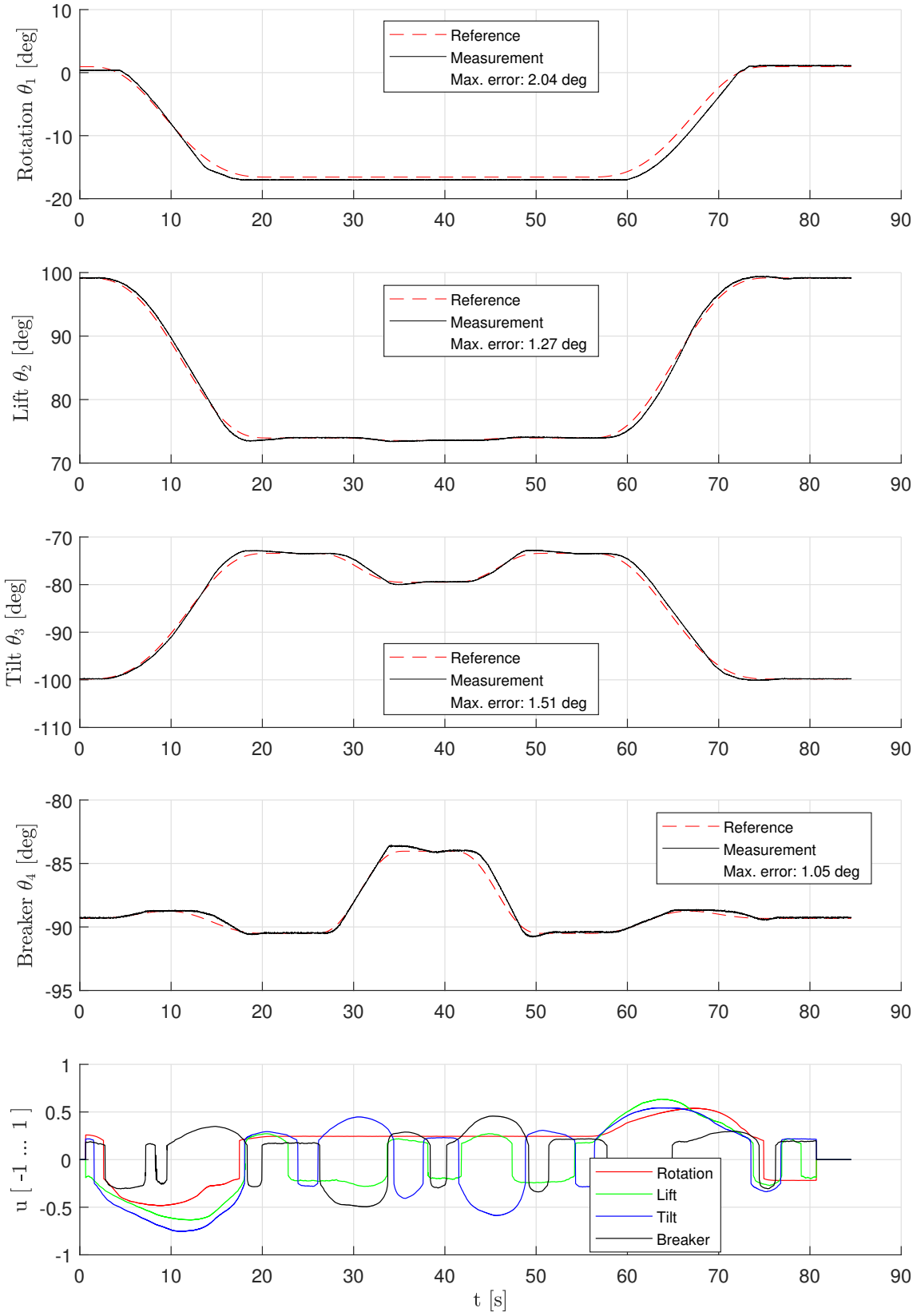

Figure B.3 *Tracking error for target point 31 with filtered P-control.*

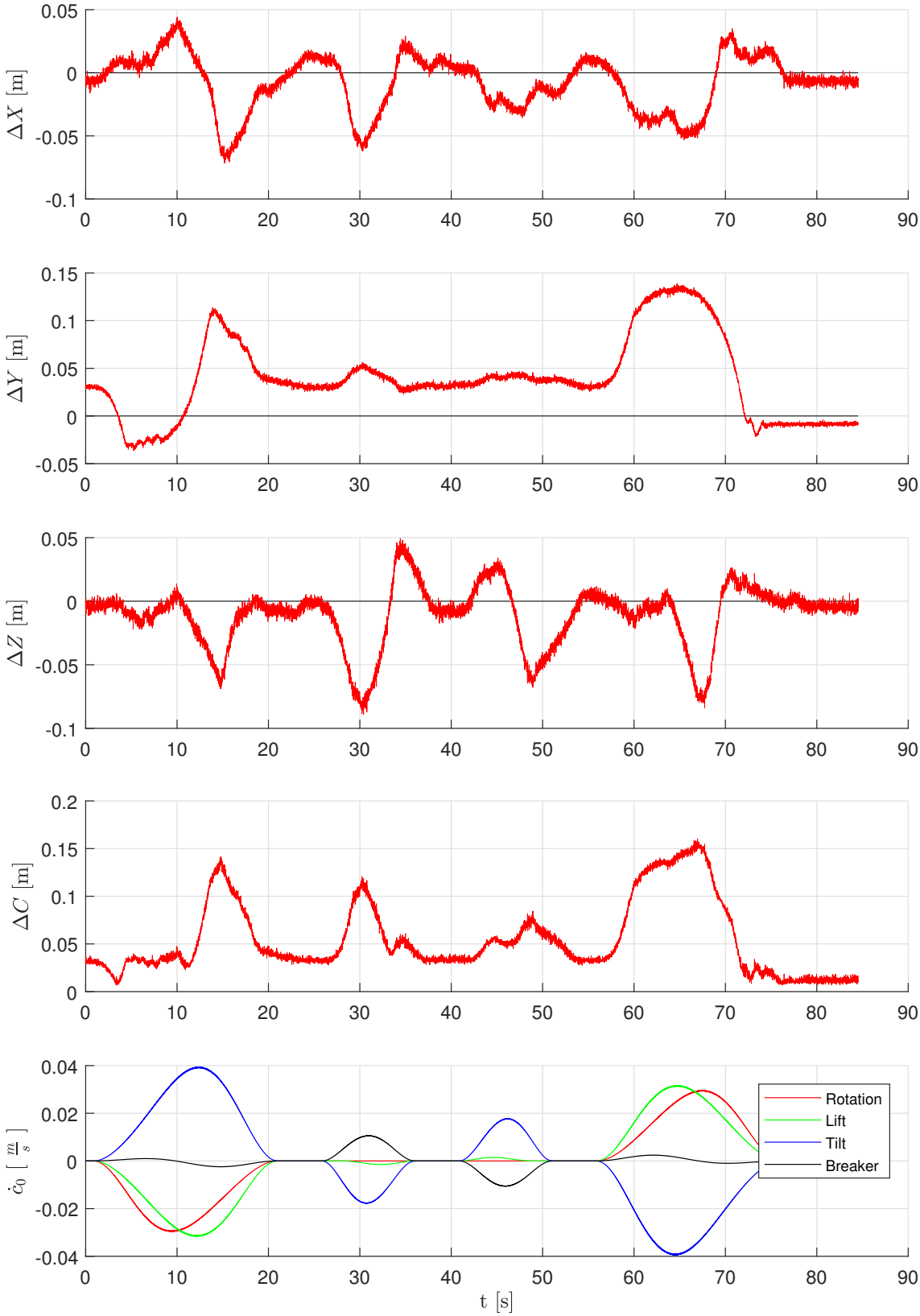

Figure B.4 *Cartesian error for target point 31 with filtered P-control.*

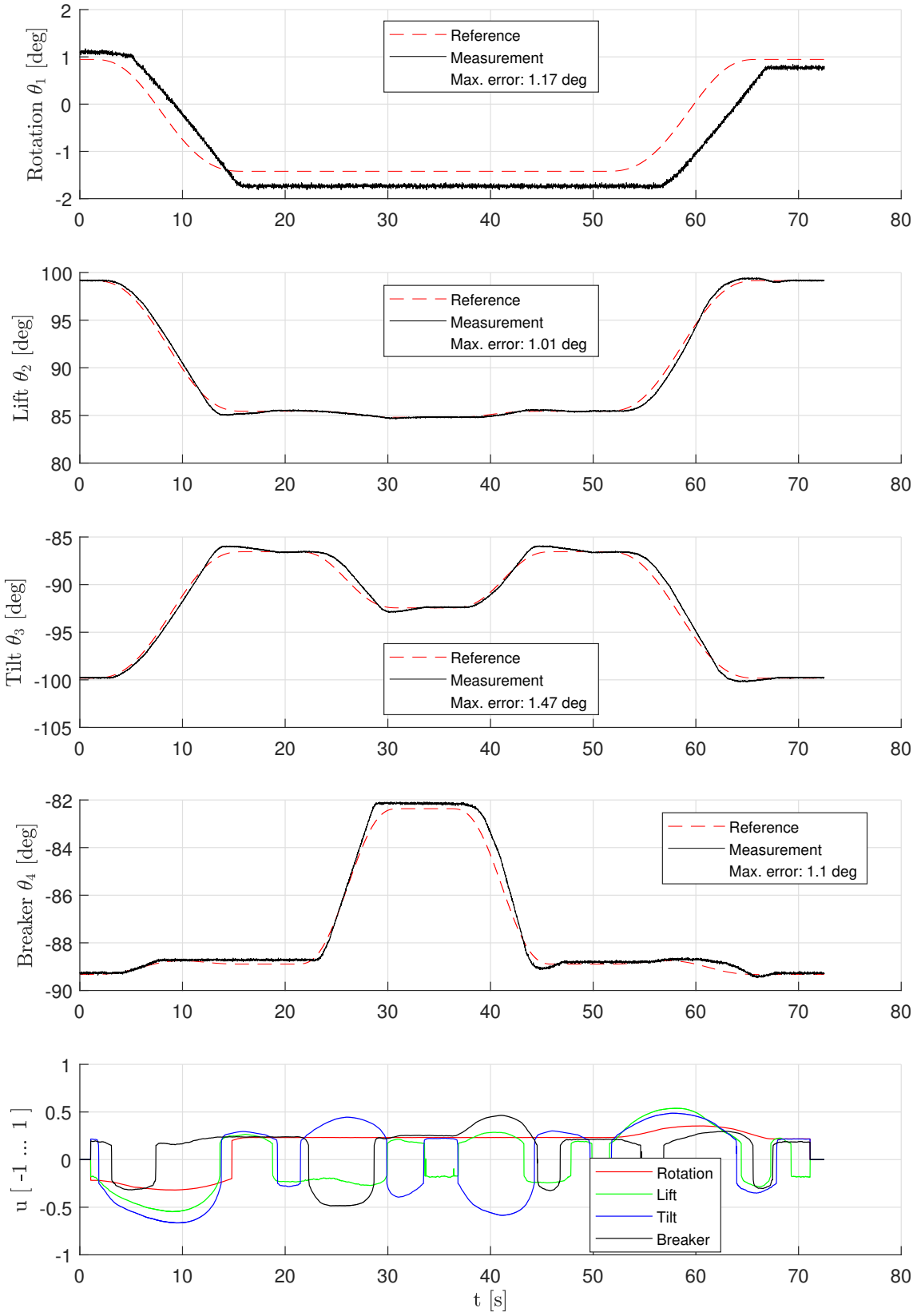

Figure B.5 *Cartesian error for target point 23 with filtered P-control.*

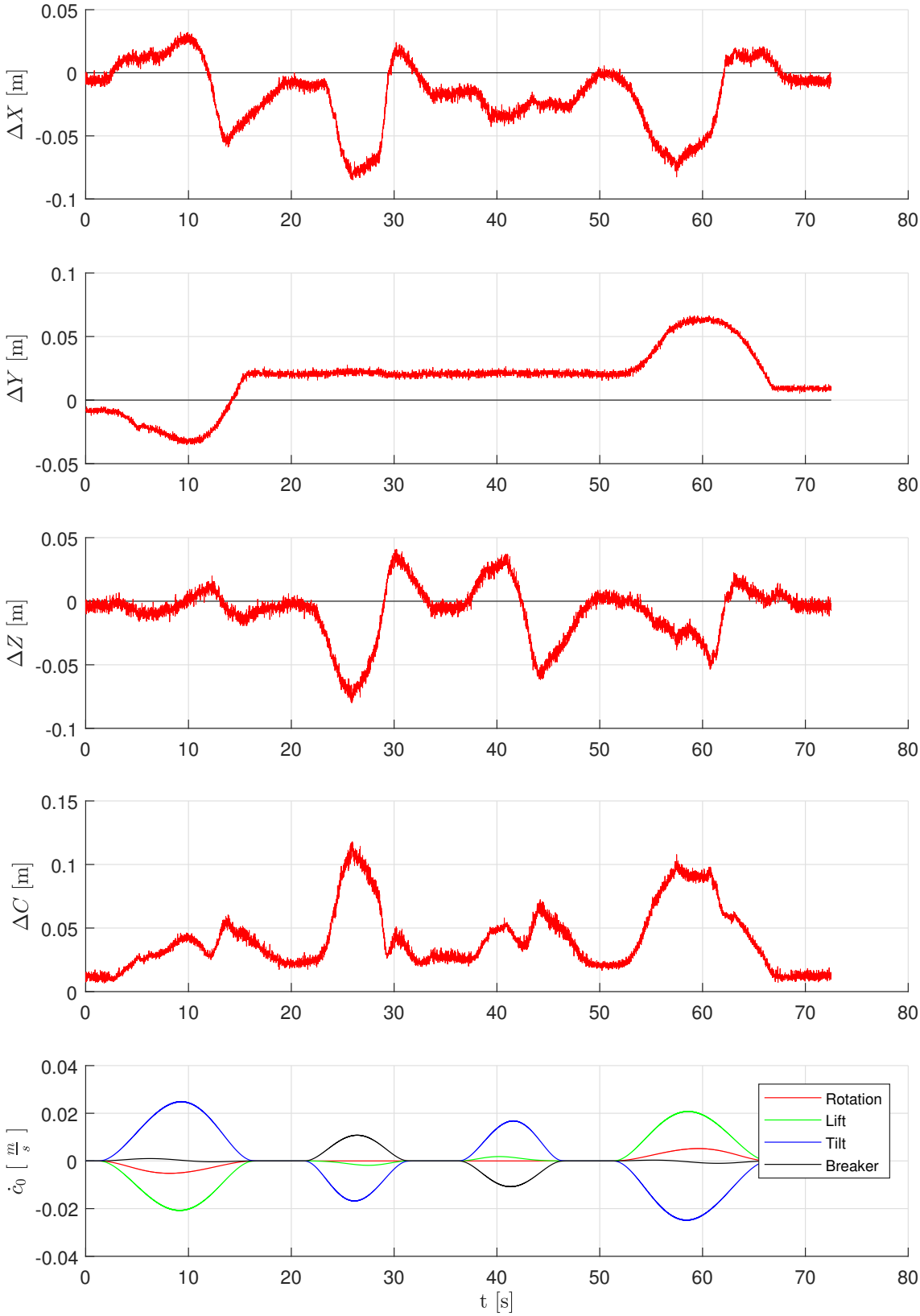

Figure B.6 *Cartesian error for target point 23 with filtered P-control.*